Journal of Geophysical Research: Solid Earth

RESEARCH ARTICLE
10.1029/2018JB016504

Key Points:
- Three-dimensional tomographic imaging reveals basin structure of the northern segments of the weakly extended Malawi Rift
- Displacement profiles for the border faults indicate Neogene-Recent throws >7 km and that they established their lengths early
- Preexisting sediments related to past rifting events are imaged beneath the Malawi Rift and may have influenced its development

Supporting Information:
- Supporting Information S1
- Data Set S1

Correspondence to:
N. J. Accardo,
nza216@psu.edu

Citation:
Accardo, N. J., Shillington, D. J., Gaherty, J. B., Scholz, C. A., Nyblade, A. A., Chindandali, P. R. N., et al. (2018). Constraints on Rift Basin structure and border fault growth in the northern Malawi Rift from 3-D seismic refraction imaging. *Journal of Geophysical Research: Solid Earth*, *123*. https://doi.org/10.1029/2018JB016504

Received 1 AUG 2018
Accepted 2 OCT 2018
Accepted article online 6 OCT 2018

Constraints on Rift Basin Structure and Border Fault Growth in the Northern Malawi Rift From 3-D Seismic Refraction Imaging

N. J. Accardo[1,2], D. J. Shillington[1], J. B. Gaherty[1], C. A. Scholz[3], A. A. Nyblade[4,5], P. R. N. Chindandali[6], G. Kamihanda[7], T. McCartney[3], D. Wood[3], and R. Wambura Ferdinand[8]

[1]Lamont-Doherty Earth Observatory, Columbia University, Palisades, NY, USA, [2]Now at the Department of Geosciences, The Pennsylvania State University, State College, PA, USA, [3]Department of Earth Sciences, Syracuse University, Syracuse, NY, USA, [4]Department of Geosciences, The Pennsylvania State University, State College, PA, USA, [5]School of Geosciences, The University of the Witwatersrand, Johannesburg, South Africa, [6]Geological Survey Department of Malawi, Zomba, Malawi, [7]Geological Survey of Tanzania, Dodoma, Tanzania, [8]Department of Geology, University of Dar es Salaam, Dar es Salaam, Tanzania

Abstract We present new constraints on rift basin structure in the northern Malawi Rift from a 3-D compressional velocity model to investigate border fault geometry, accommodation zone structure, and the role of preexisting structures underpinning this rift system. The velocity model uses observations from the first wide-angle refraction study conducted using lake-bottom seismometers in one of the East African great lakes. The Malawi Rift is flanked by basin-bounding border faults and crosses several significant remnant structures, making it an ideal location to investigate the development of normal faults and their associated basins. The 3-D velocity model reveals up to ~5 km of synrift sediments, which smoothly transition from eastward thickening against the Livingstone Fault in the North Basin to westward thickening against the Usisya Fault in the Central Basin. Greater than 4 km of sediment are imaged within the accommodation zone pointing to the early development of the border faults. We use new constraints on synrift sediment thickness to construct displacement profiles for both faults. Both faults accommodate large throws (>7 km) consistent with their significant lengths. The dimensions of these faults are close to or larger than the maximum size predicted by models of fault growth. The presence of an intermediate velocity unit with velocities of 3.75–4.5 km/s is interpreted to represent sediment deposits beneath Lake Malawi from prior rifting in the Permo-Triassic (Karoo) and/or Cretaceous-Paleogene. The distribution of preexisting basins implied by these sediments may help account for changes in intrabasinal faulting and border fault development between the two basins.

1. Introduction

Border faults along the Western Rift of the East African Rift System (EARS) formed within cold, strong lithosphere and have achieved fault lengths of over 100 km, making them some of the largest normal faults in the world (Ebinger et al., 1999). Competing models for fault growth predict different relationships between fault length, fault displacement, seismogenic layer thickness, and surface processes (e.g., Buck, 1993; Cowie & Scholz, 1992; Dawers & Anders, 1995; Olive et al., 2014), which have direct implications for the initiation and evolution of rift systems as well as present-day seismic hazards. The isolated-fault model (e.g., Cartwright et al., 1995; Dawers et al., 1993; Dawers & Anders, 1995) suggests that displacement should scale linearly with length, while the constant-length model (e.g., Curry et al., 2016; Morley, 2002; Nicol et al., 2005; Walsh et al., 2002) suggests that fault length is established early, such that the ratio of displacement to length can vary (for a review see Jackson et al., 2017). These end-member models make different predictions for the distribution of extension along border faults, and the structure of accommodation zones, where strain is transferred between adjoining border fault bounded basins. Although several studies evaluate border and intrabasinal fault dimensions along the Western Rift (e.g., Jackson & Blenkinsop, 1993, 1997; Morley et al., 1992), our understanding of these fault systems and implications for controls on fault development have been hampered by a paucity of constraints on total fault throw and how it varies along and between faults in this and other rift systems.

Models for normal fault behavior have direct implications for the evolution of rift basins and the lifespan of these large border faults. Border faults accommodate significant extensional strain in the brittle crust. Several

primary factors control the border fault dimensions including the elastic thickness, or integrated strength envelope, of the continental lithosphere (e.g., Hayward & Ebinger, 1996; Jackson & Blenkinsop, 1997). As rifting progresses, strain migrates inward onto intrabasinal structures as has been shown in many rifts including in Greece (Goldsworthy & Jackson, 2001) and the Main Ethiopian Rift (Ebinger & Casey, 2001). Modeling studies have proposed different theoretical limitations on border fault offset before faults become mechanically unfavorable and may be abandoned in favor of new faults (e.g., Olive et al., 2014; Scholz & Contreras, 1998), yet limited observations are available on the cumulative offset on large border faults at the scale of the faults studied here (owing to the few number of faults of this scale as well as difficulty in accessing their locations) to test these models.

Extensive debate also surrounds the role of inherited structures in the rifting process and suggests that their influence may be scale dependent (e.g., Kirkpatrick et al., 2013). At the continental scale, rift systems often develop in regions that are mechanically weaker than the surrounding lithosphere (e.g., Corti et al., 2007; Delvaux, 2001; McConnell, 1972; Nyblade & Brazier, 2002; Tommasi & Vauchez, 2001). At the basin scale, studies suggest that favorably oriented preexisting structure or basement fabrics may favor normal fault formation and growth (e.g., Ebinger et al., 1999; Fagereng, 2013; Kinabo et al., 2008; Morley, 2010; Ring, 1994), and structures that obliquely cross a rift could limit fault length, impact fault polarity or lead to the formation of complex intrabasinal structures (Corti et al., 2007; McCartney & Scholz, 2016; Versfelt & Rosendahl, 1989). Preexisting structures and basement fabrics have also been proposed to influence the location and architecture of accommodation zones (e.g., Versfelt & Rosendahl, 1989). In detail, the nature and degree of influence of preexisting structures is highly variable (e.g., Kirkpatrick et al., 2013). Evaluating the presence and influence of preexisting structures is crucial to deciphering how extension is accommodated on the scale of individual faults, rift basins, and entire rift systems. Processes associated with present-day extension often obscure preexisting structures, making it difficult to evaluate their influence.

This paper presents results from the first seismic refraction survey using lake-bottom seismometers undertaken in an East African rift lake. We conduct 3-D first-arrival travel time tomography to constrain basin structure within the weakly extended Malawi Rift with the aim of constraining patterns of extension and sedimentation within rift segments and the accommodation zones between them, and the role of preexisting structures by determining the structure of the rift basins and uppermost crust. Our investigation provides new insight into border fault geometry, accommodation zone structure, and the role of preexisting structures underpinning this rift system.

2. Geologic Background

2.1. The EARS

The EARS developed within old, cold, thick lithosphere characterized by large values of effective elastic thickness (T_e) and lithospheric strength (e.g., Ebinger et al., 1999; Pérez-Gussinyé et al., 2009; Stamps et al., 2014). The EARS bifurcates around the Archean Tanzanian Craton into the Western and Eastern Rifts (see inset in Figure 1a), with both rifts developing within thinner, and mechanically weaker, Proterozoic orogenic belts (for a review see Fritz et al., 2013). The alignment of rift basins and Proterozoic mobile belts suggests the large-scale control of preexisting lithospheric structures on rift evolution (e.g., Corti et al., 2007; Nyblade & Brazier, 2002). At smaller scales, the relationship between rifting and preexisting lithospheric heterogeneities appears more complex. The EARS developed within terranes that host major shear zones and remnant extensional/orogenic structures with variable orientations with respect to present-day extension (e.g., Catuneanu et al., 2005; Fritz et al., 2013), and debate continues concerning how these structures may influence basin development and fault growth (e.g., Corti et al., 2007; Daly et al., 1989; Ebinger et al., 1997; Fagereng, 2013; Kinabo et al., 2008; Smith & Mosley, 1993).

The Western Rift is characterized by a series of $>$100-km-long asymmetric basins flanked by broad uplifts, occasionally with alternating polarity (e.g., Rosendahl et al., 1992). Estimates of crustal stretching from balanced cross sections of rift profiles, forward models of basin and flank morphology, and seismic imaging indicate $\leq$20% crustal thinning, or about 10 km of opening in sectors of the Western Rift (Ebinger et al., 1991; Morley, 1988; Wölbern et al., 2010). These weakly extended rift basins are commonly filled by narrow and deep freshwater lakes (e.g., Soreghan et al., 1999). While magmatism is widespread in rift sectors north

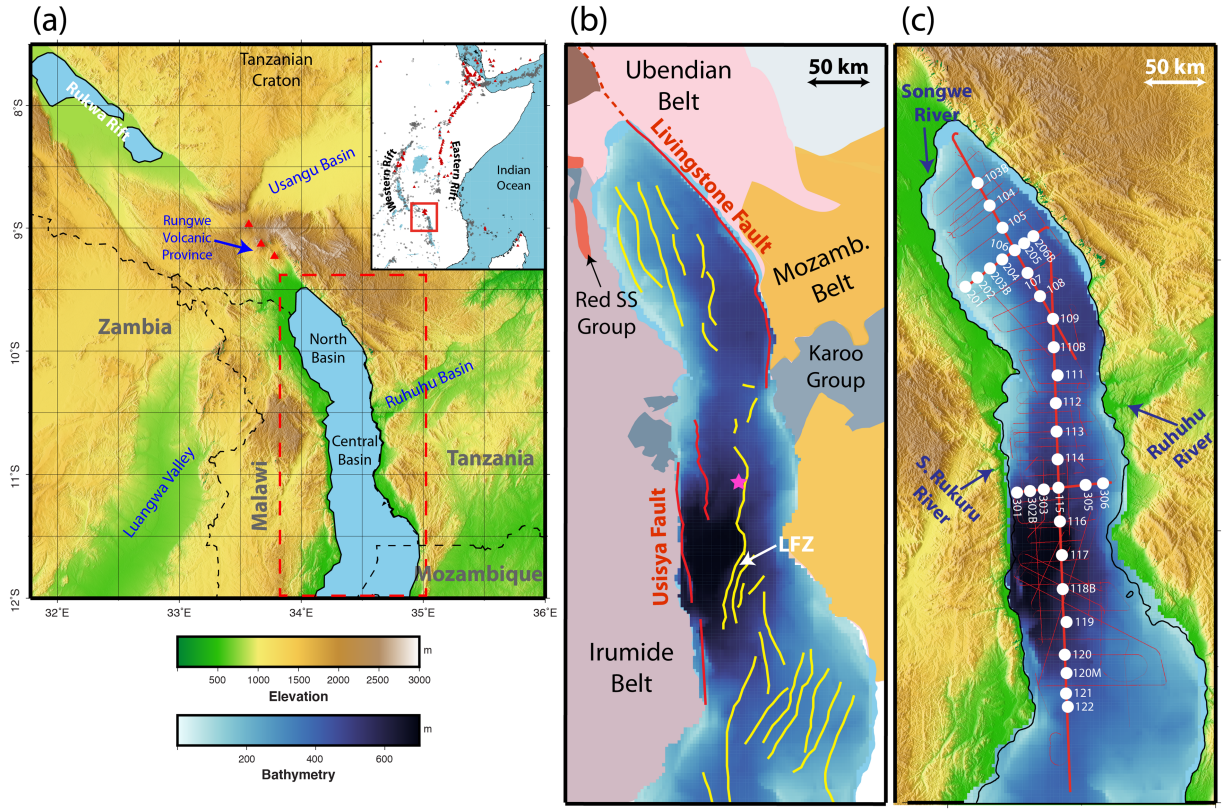

Figure 1. (a) Overview figure of the study region with locations of interest labeled. Red triangles indicate Quaternary-Recent volcanoes. The location of the study area is shown within East Africa (regional seismicity is shown as gray circles and volcanoes as red triangles) in the inset. The location of maps in (b) and (c) are shown by the dashed red rectangle. (b) Simplified onshore geology of the northern Malawi Rift. The Irumide, Ubendian, and Mozambique Proterozoic mobile belts are shown as well as Karoo group (Carboniferous-Permian) and Cretaceous Red Sandstone (SS) group sediments. Geologic units were mapped following Bennett (1989), Delvaux (2001), Pinna et al. (2004), Roberts et al. (2010), and Fritz et al. (2013). Intrabasin faults (yellow) and the border faults (red) are shown from Mortimer et al. (2007), Lyons et al. (2011), and McCartney and Scholz (2016). All of the major intrabasin faults within Lake Malawi are thought to be normal faults. The pink star shows the location of the profiles shown in Figure 2. (c) Map detailing the Study of Extension and maGmatism in Malawi and Tanzania active-source experiment. Red lines indicate the lines were reflection/refraction data were acquired. Lake-bottom seismometers locations are shown by the white circles, and instrument names are labeled. Blue arrows indicate where rivers enter Lake Malawi. Bathymetry of Lake Malawi is shown in both (b) and (c).

and east of the Tanzania craton, the Western Rift is relatively magma poor, with volcanism limited to isolated, volumetrically small volcanic centers (Furman, 2007).

Few data points exist to date the onset of rifting in the deep Western rift lakes. Extrapolations of present-day sedimentation rates suggest rifting initiated by ~12 Ma (for a review see Ebinger & Scholz, 2012). However, recent dating of volcanic rocks from the Rungwe volcanic province (RVP, located at the northern end of the Malawi Rift) yield ages of ~17 Ma (Mesko et al., 2014; Rasskazov et al., 2003), and dating of airfall deposits in the Rukwa Rift (Figure 1a) suggests that magmatism started as early as 26 Ma (Roberts et al., 2012). Together these results indicate that extension in the Western Rift may have begun earlier than previously thought.

2.2. Lake Malawi and the Malawi Rift

The Malawi Rift in the southern EARS is a seismically active, magma poor, weakly extended continental rift. Like other African rift lakes, Lake Malawi is narrow (25–80 km wide) and deep (maximum water depth is ~700 m; Figure 1). Border fault-bounded half grabens partition the Malawi Rift into three basins (North, Central, and South) separated by accommodation zones whose geometries were poorly constrained by earlier seismic reflection surveys (e.g., Scholz, 1989).

These basins developed within and at the boundaries of different Proterozoic terranes (e.g., Fritz et al., 2013; Hanson, 2003; Figure 1b). The Malawi Rift crosscuts two large-scale Permo-Triassic (Karoo) basins: the Ruhuhu

Basin, which intersects the rift at the accommodation zone between the North and Central Basins (Ebinger et al., 1987; Versfelt & Rosendahl, 1989; Figure 1a), and the Maniamba Trough, which intersects the rift to the east between the Central and Southern basins (Catuneanu et al., 2005). Karoo-age and Cretaceous-Paleogene Red Sandstone sediments associated with prior rifting episodes outcrop along the western edge of the RVP continuing toward the Rukwa Rift (e.g., Jacobs et al., 1990; Roberts et al., 2010).

2.3. The North and Central Basins of Lake Malawi

For this study, we focus on the North and Central Basins of Lake Malawi. Seismic reflection images show that the North Basin represents a type example of a half-graben structure, with sediments thickening eastward toward the west-dipping border fault (Livingstone Fault; e.g., Mortimer et al., 2007; Scholz, 1989). The Livingstone Fault continues for more than 120 km along the eastern lakeshore of the North Basin (Wheeler & Karson, 1989), with the fault trace terminating in the south near the Ruhuhu Basin. The Livingstone Fault continues onshore ~30 km north of Lake Malawi (Ebinger et al., 1993; Wheeler & Rosendahl, 1994; Figure 1a). While the border faults that bound the Central and South basins of the Malawi Rift are oriented approximately N-S, orthogonal to the inferred E-W extension direction (e.g., Stamps et al., 2014), the strike of the Livingstone Fault is NNW-SSE. In detail, the trace of the Livingstone Fault contains two small ($<$5 km) steps that divide it into three ~30- to 40-km-long segments (Mortimer et al., 2007). The hanging wall is cut by synthetic intrabasinal faults both beneath the lake and onshore to the north (i.e., Mbaka Fault), some with significant offset (Ebinger et al., 1993; Mortimer et al., 2007; Specht & Rosendahl, 1989; Wheeler & Rosendahl, 1994).

Despite previous studies, much uncertainty remains concerning the amount and distribution of sediment within the North Basin. Previous seismic reflection imaging (hereafter termed legacy) included Project PROBE, which collected data over the entire lake in the 1980's (e.g., Scholz, 1989), and high-resolution single channel programs focused on delta structures in both basins in 1992 and 1995 (Scholz, 1995a, 1995b). While these data provided important constraints on shallow sedimentary structure and faulting, depth penetration was limited by small source volumes and did not clearly identify basement reflections (e.g., Flannery & Rosendahl, 1990; Mortimer et al., 2007). Models of gravity data constrained by seismic reflection data estimate 4–5 km of total sediment in the North Basin (Ebinger et al., 1991, 1993), but these data could not discriminate between prerift and synrift sediments.

The Central Basin is bound on the west by the ~140-km-long Usisya border fault, an east-dipping array of faults (Figure 1b). The Usisya border fault comprises three fault segments, each 40–60 km long, which are offset by ~10 km with respect to each other (e.g., Contreras et al., 2000; Ebinger et al., 1987; Scholz, 1989; Soreghan et al., 1999). These offsets are larger than the steps that separate the segments of the Livingstone Fault. Prior studies have identified a significant relay-ramp structure that connects the north and central segments (e.g., Ebinger et al., 1987; Scholz, 1989). Like the North Basin, the Central Basin represents a single half-graben basin but exhibits more complex intrabasinal faulting. Previous reflection seismic studies have imaged the structurally complex, north-northwest dipping Lipichilli Fault Zone that extends for ~28 km across the southern edge of the basin (Figure 1b; McCartney & Scholz, 2016; Scholz, 1989). Previous studies using PROBE seismic reflection data in the Central Basin could not confidently identify crystalline basement in many areas. Because these data were acquired with a short streamer (maximum length 1,200 m), they cannot constrain velocities for most of sedimentary section, thus estimating sediment thickness from two-way travel time (TWTT) required assuming a velocity (e.g., 2 km/s; Contreras et al., 2000; Wheeler & Karson, 1989). The deepest bathymetry within Lake Malawi is found within the Central Basin, in a region bounded to the west by the central segment of the Usisya border fault and the east by an intrabasinal high (Figure 1b). Some studies suggest that a second border fault bounds the eastern side of the southern Central Basin, termed the Mbamba Fault (e.g., Flannery & Rosendahl, 1990; Laó-Dávila et al., 2015; Mortimer et al., 2016). However, McCartney and Scholz (2016) suggest that this feature is not a rift border fault based on the absence of clear patterns of eastward thickening sediment expected for hanging wall subsidence.

The character of the accommodation zone between the North and Central Basins and the manner in which strain is transferred between the Livingstone and Usisya Faults remains enigmatic (Flannery & Rosendahl, 1990). One PROBE seismic reflection line images a possible structural high embedded within an area of overall low relief (Specht & Rosendahl, 1989). Studies of the Malawi Rift have suggested that the presence of the Ruhuhu Basin, which intersects the rift at the accommodation zone, influenced the location and structure of

the accommodation zone between the North and Central Basins (e.g., Versfelt & Rosendahl, 1989). However, seismic reflection data do not image the base of synrift sediments over much of this region and are not able to image prerift sediments anywhere beneath the Malawi Rift (Flannery & Rosendahl, 1990) thus limiting our understanding of the role of preexisting structures in the nature and development of the accommodation zone.

3. Data and Methods

3.1. SEGMeNT Active-Source Seismic Experiment

An active-source seismic experiment was conducted in the North and Central Basins of Lake Malawi in the spring of 2015 as a part of the multidisciplinary Study of Extension and maGmatism in Malawi and Tanzania (SEGMeNT) project (Shillington et al., 2016). Thirty-two lake-bottom seismometers (LBS) were deployed in February 2015 by the F/V *Ndunduma*. The LBS array comprised 26 Scripps Institute of Oceanography (SIO) four-component (three-component geophone and hydrophone) short-period instruments and six SIO four-component (three-component seismometer and differential pressure gauge) broadband instruments. The instruments recorded data at 100 Hz (broadband) and 200 Hz (short period). The 26 short-period instruments were recovered in April 2015 by the F/V *Ndunduma*, and the six broadband instruments were recovered in November 2015 by the M/V *Chilembwe*, and thus all instruments recorded the entire active-source seismic program. Instruments were deployed in 200–650 m of water and along three main transects (see Figure 1c) with a spacing of ~7–15 km.

During a 29-day cruise aboard the M/V *Katundu* in March 2015, seismic reflection data were acquired, and seismic sources were generated for the wide-angle reflection/refraction study, which is the focus of this paper. The primary acoustic source for the refraction work consisted of six air guns from the Geological Survey of Greenland and Denmark and Aarhus University with a combined shot volume of 2,580 $in.^3$ (42,278.63 cm^3) firing at a pressure of 180 bars. Shot spacing for the refraction work was 250 m to mitigate previous shot noise. In total, we acquired $>$1,500 km of data at this large shot volume including the primary profile lines, additional refraction lines, turns between reflection lines, and during streamer and ship maintenance.

Over 2,000 km of seismic reflection data were acquired with a variety of source configurations (volumes between 500 $in.^3$ [8,193.53 cm^3] and 1,580 $in.^3$ [25,891.56 cm^3]) fired at pressures of ~120 bars. Shots were recorded on a digital Hydroscience Technologies streamer from Syracuse University with a group interval of 12.5 m, yielding a common midpoint spacing of 6.25 m. Streamer length was usually 1,200–1,500 m, though a few lines were acquired with a much shorter streamer ($<$700 m) configuration. Shot spacing during the reflection acquisition varied between 12 and 50 m. LBS were in place for the entirety of the *Katundu* cruise and recorded all shots. Whereas the larger volume shots were recorded on LBS to offsets $>$230 km, the smaller volume shots were generally limited to offsets of ~25 km due to interference from previous shot noise.

3.2. Seismic Reflection Processing

Here we present three examples of seismic reflection profiles from the SEGMeNT project for comparison with velocity models derived from seismic refraction data. Processing of these data involved the following steps: geometry assignment and common midpoint binning, data cleaning, suppression of lake-bottom multiples using surface-related multiple elimination (Verschuur et al., 1992), velocity analysis, normal moveout, stacking, and poststack Kirchoff time migration (McCartney et al., 2016; Shillington et al., 2016). The quality of these images is better than older legacy data, primarily owing to the larger source volume used in this study. However, these data can only constrain velocity to maximum depths of ~1,200–1,500 m due to the limited aperture of the streamer. Thus, they cannot constrain velocities throughout the entire sedimentary section and sediment thickness. As discussed in section 5.1, the ability of these processed seismic reflection data to image of the base of synrift sediments varies throughout the basin, and no prerift sediments can be imaged, similar to legacy data sets.

3.3. Seismic Refraction Data Processing and Phase Interpretation

Processing of LBS data was conducted using the Seismic Unix software package (http://www.cwp.mines.edu/cwpcodes/) and involved the following steps: (1) minimum-phase band-pass filter with corners at 2, 4, 15, and 20 Hz; (2) reduction velocity of 6 km/s; (3) trace balancing; and (4) offset-variable gain to all traces. On five of

Table 1
Instrument Names, Locations, Total Number of Picks, Chi-Square, and RMS Values Associated With the Final Velocity Model

LBS	Lon	Lat	Water depth (m)	# Picks	Chi squared	RMS (s)
122	34.448	−11.648	458	765	0.6453	0.0717
121	34.441	−11.598	450	931	1.9746	0.1259
120 M	34.443	−11.523	475	1,058	0.7513	0.0814
120	34.437	−11.456	518	1,576	0.6642	0.0911
119	34.444	−11.336	560	1,615	0.9067	0.1134
118B	34.430	−11.214	605	2,628	1.0306	0.1156
117	34.427	−11.089	683	911	0.8836	0.0682
116	34.419	−10.965	679	1,600	0.7271	0.0758
301	34.259	−10.859	500	1,598	1.7035	0.1372
302B	34.308	−10.853	512	2,110	1.8653	0.1188
303	34.359	−10.847	584	2,048	0.4889	0.0794
115	34.414	−10.841	563	2,051	1.1493	0.0923
305	34.523	−10.829	490	849	0.8001	0.0995
306	34.579	−10.825	397	1,120	3.6149	0.1903
114	34.410	−10.737	514	1,718	0.6533	0.0869
113	34.407	−10.633	472	1,892	0.5995	0.0716
112	34.403	−10.529	454	998	1.3684	0.1226
111	34.410	−10.426	458	1,332	1.1896	0.0993
110B	34.396	−10.322	485	1,595	0.3902	0.075
109	34.393	−10.218	492	1,578	0.7875	0.1077
108	34.345	−10.134	466	1,402	1.0803	0.1103
201	34.066	−10.098	132	571	0.3309	0.0626
202	34.111	−10.065	212	1,293	0.6341	0.0877
203B	34.158	−10.031	312	1,135	1.6518	0.1372
107	34.298	−10.048	450	1,561	0.8802	0.0876
204	34.204	−9.997	386	1,556	0.9535	0.0975
106	34.250	−9.963	375	1,476	0.4034	0.0668
205	34.286	−9.939	400	970	0.621	0.0765
206B	34.320	−9.912	402	1,449	0.8549	0.0954
105	34.205	−9.881	331	1,271	0.7602	0.0824
104	34.157	−9.799	321	1,545	1.0694	0.0934
103B	34.112	−9.716	265	974	1.8801	0.113

Note. LBS = lake-bottom seismometers; RMS = root-mean-square.

the 32 LBS, we utilized the hydrophone channel rather than the vertical-component geophone due to significantly higher signal-to-noise ratio. Instruments were not relocated because water depths are relatively shallow (<700 m), and relocation tests on instruments did not yield significantly different positions. The times of direct arrivals on near-offset traces indicate that the instrument deployment positions were consistent with the data.

First arrivals were picked on all instruments to offsets of 50 km (Table 1). Arrivals were visible to offsets >220 km, but we did not use them in this study, which is focused on basin structure. The uncertainty of each travel time pick was assigned via visual inspection. Uncertainties ranged from 25 to 200 ms with a median uncertainty of ~100 ms. The largest uncertainties were limited to picks at far offsets on the reflection lines (~25-m shot spacing) where previous shot noise was significant. To ensure that picks from lines with shorter shot intervals did not dominate the inversion, we decimated our initial data set (101,496 picks) such that picks had a minimum spacing of 150 m along all profiles leading to a data set of 45,208 picks that were used in the inversion (Table 1). We made all picks within the Universal Transverse Mercator (UTM) coordinate system and then applied a linear operator to convert to a local coordinate system for the remainder of this study. The origin of the local coordinate system is −12.03N, 33E. We set the $Z = 0$ km in the local coordinate system to correspond to the elevation of the surface of Lake Malawi, which is at 454 m above sea level.

We took several steps to ensure high-quality, accurate picks. In 2-D refraction work, reciprocity checks are commonly used to ensure consistent phase identification (e.g., Zelt, 1999). While this approach is applicable to our three 2-D refraction lines, the 3-D experiment geometry precludes reciprocity checks for most picks. To ensure consistent phase identification, we checked that picks at line intersections were consistent for a given station. Additionally, after picking all data, we visually inspected maps of travel time picks for each individual instrument in unreduced time to ensure that there were no abrupt lateral variations in travel time and thus the same first-arriving phase was consistently picked (see supporting information).

3.4. Monte Carlo First-Arrival Inversion Methodology

To obtain a 3-D model of *P* wave velocity structure based on travel time picks, we implemented a Monte Carlo methodology using the iterative first-arrival tomographic inversion code FAST (First Arrival Seismic Tomography; Zelt & Barton, 1998). A Monte Carlo approach to refraction imaging involves both perturbing the data set of travel time picks (adding random noise scaled by pick error) and constructing numerous randomized initial models to perform the inversion (e.g., Delescluse et al., 2015; Korenaga et al., 2000, Watremez et al., 2015; Zhang & Toksoz, 1998).

3.4.1. Construction of Initial Models and Perturbed Travel Times

We constructed 200 unique 3-D starting models. Each initial model is parameterized with three layers where Layer 1 represents the water layer of Lake Malawi, which was constructed by fitting a surface to the estimated lake bottom in depth from >10,000 km of existing reflection lines (Figures 1b and 1c; Lyons et al., 2011) and assigned a velocity of 1.5 km/s. Layers 2 and 3 are intended to approximate sedimentary and crustal layers, respectively. All models extend from the lake surface to a depth of 15 km. To construct the 200 starting models, we randomly perturbed three defining parameters of the velocity model: (1) velocity at the base of Layer 2, (2) velocity at the base of Layer 3, and (3) the ratio between the thickness of Layer 1 (held constant) and the thickness of Layer 2. The ratio between the thicknesses of Layer 1 and Layer 2 is always >1 meaning that water depth and the thickness of the sedimentary layer is correlated. Parameters were varied between

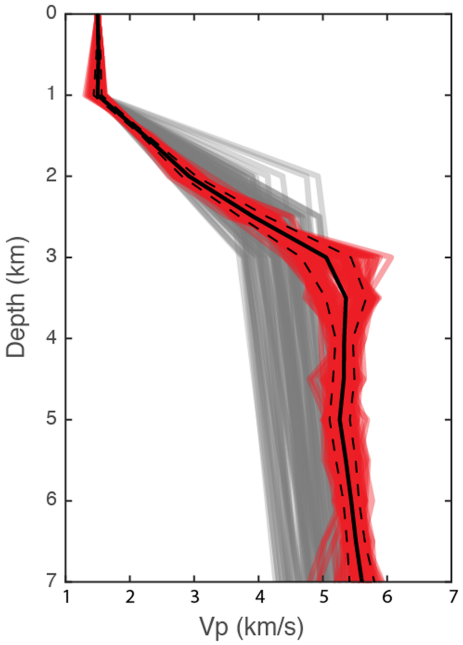

Figure 2. Comparison of all 1-D *V*p profiles for a given location from the initial models (gray lines) and the final models (red lines). One hundred five total models are shown. The black solid line indicates the average of all final velocity models, and the black dashed lines indicate one standard deviation around the mean velocity. The location where these profiles were taken is shown by the pink star in Figure 1b.

30% and 50% (Figure 2). For each initial model, we constructed a modified data set of travel time picks defined as the original travel time picks with added random Gaussian noise, where the standard deviation of the distribution was equal to the estimated pick uncertainty (e.g., Zhang & Toksoz, 1998).

3.4.2. Travel Time Tomography With FAST

The FAST tomographic code (Zelt & Barton, 1998) aims to find the model with the least amount of structure that fits the data within their uncertainties. This is a linearized inversion where the velocity model and raypaths are updated after each iteration until the normalized misfit (χ^2) equals 1 or data misfits stop improving. χ^2 is defined as

$$\chi^2 = \frac{1}{N}\Sigma\frac{\left(t_{\text{obs}} - t_{\text{pre}}\right)^2}{\sigma^2_{\text{obs}}}, \quad (1)$$

where t_{obs} and t_{pre} represent the observed and calculated arrival times, respectively; N represents the total number of picks; and ?$_{\text{obs}}$ represents the estimated uncertainty of the pick.

The forward step of FAST utilizes the 3-D finite difference Eikonal solver of Vidale (1990) on a 0.5-km grid. For the inverse step, cell sizes are made larger ($3 \times 3 \times 0.5$ km in the x, y, and z directions, respectively) as larger cells have increased control on model parameters. Model updates during the inversion are calculated via a least squares conjugate gradient method. The trade-off parameter, ?, which controls the regularization between data misfit and model smoothness, is systematically reduced with each iteration. This process stabilizes the inversion by first constraining long-wavelength structure before allowing finer structure in later iterations. We applied constraints on vertical and horizontal smoothness to ensure realistic Earth structure. Smoothing increases with depth in the model, with the lower 7.5 km having a 50% larger smoothness weight. Typical inversions required four to five iterations before they were stopped because either χ^2 reached 1 or the data misfit stopped improving (Figure 3). Of the 200 models, 198 models successfully converged. We present a single final model that is constructed by averaging all models with a $\chi^2 < 1.25$ (105 models), and we limit our discussion of results to this averaged model. To confirm the fit of this average model to the data, we trace rays through the model (Figure 4) and calculate predicted travel times, χ^2 and root-mean-square (RMS) misfit (Figures 4 and 5). To quantify uncertainty, we calculated the standard deviation of the final velocity in each grid cell and present it as a percent uncertainty of the final velocity.

4. Results

The 3-D velocity model provides unique constraints on the deep basin structure of the northern Malawi Rift. The final model has a $\chi^2 = 1.08$, $RMS = 102$ ms, and traces 93.6% of all rays (Figures 6 and 7). Uncertainty estimates broadly mirror hit count and are lowest within the center of the model (<2%), particularly in the locations of slow velocities, interpreted as sedimentary basins. Uncertainties increase around the edges of the model and at greater depths. Larger uncertainties are also associated with parts of the model with large velocity gradients (i.e., the boundary between sediments and crystalline basement; Figures 7d, 7f, and 7h), which we attribute to the limited ability of the smooth first-arrival tomography method to recover sharp changes in velocity.

Our model reveals clear differences in the velocity structure between the North and Central Basins (Figure 6). In the North Basin, a shallow layer characterized by slow velocities (Vp < 3.75 km/s) thickens to the east toward the Livingstone border fault (Figures 6, 7b, and 7d). The deepest occurrence of slow velocities is observed near the southern part of the Livingstone Fault (Figure 7d); this region is also the location of the deepest bathymetry within the North Basin. A fast velocity ridge in the center of the basin that roughly parallels the border fault separates the swath of low velocities against the border fault from a more limited

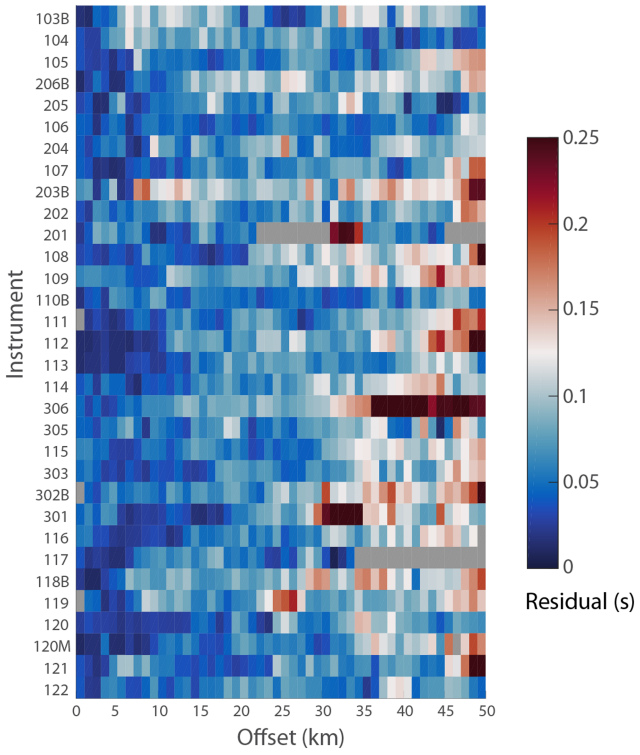

Figure 3. Data misfit for the final model shown for each instrument (*y* axis) against the offset of the air gun shot. Gray boxes indicate where no picks were available for instruments. Locations of the instruments are given in Figure 1c.

region of slow velocities to its west (Figures 6a, 6b, and 7c). West of this fast-velocity ridge, low-velocity material thins and shallows to the west consistent with the geometry of a typical half-graben basin (Figures 6a and 7c). In the northern part of the North Basin, a circular region (diameter ~20 km) of slow velocities persists to depths >4 km. This feature is associated with abundant ray coverage (>50 rays), low uncertainty (Figure 6d), and clear changes in observed arrivals in LBS data (e.g., Figure 4c); thus, we consider it robust. At the southern end of the North Basin (south of $Y = 175$), the package of slow-velocity material shifts sinuously westward until it abuts the relay ramp between northern and central segments of the Usisya Fault at $Y = 155$. No high-velocity ridges or other structures are observed within the accommodation zone. Within this zone, slow velocities can be seen to thicken toward both the east and west sides of the basin (Figure 7e).

The Central Basin is significantly more complex than the North Basin in both the types of structures present and the strike of the structures. Layers with relatively slow velocities thicken against each segment of the Usisya Fault (Figures 7e–7g). This slow-velocity material is bounded on the east by a series of faults that define an intrabasinal high (Figure 6d). Slow velocities persist to depths >5 km within the region bounded by the central segment and this intrabasinal high (between $Y = 80$ and $Y = 120$, Figures 6a, 6d, and 6g), which corresponds to the deepest water in Lake Malawi (698 m). The intrabasinal high is expressed in these profiles as a high-velocity structure ($Vp > 5.5$ km/s; Figure 7f) separating the region of low-velocity material against the border fault to the west and a shallower section of slow-velocity material to the east. Other complex intrabasinal structures in the Central Basin that were previously recognized in legacy seismic reflection data can also be observed in our models (e.g., the Lipichilli Fault Zone; McCartney et al., 2016; Figures 1b and 7g). In the southern Central Basin, slow velocities are nearly absent at depths >2.5 km, and instead velocities remain fast ($Vp > 5.5$ km/s; $Y = 0$–50; Figure 6a). In the northern Central Basin and accommodation zone ($Y = 130$–175), cross sections reveal a relatively thick (~2 km) layer with velocities intermediate between those expected for synrift sediments and crystalline basement (~3.75–4.5 km/s, Figures 7e and 7f). This material is clearly distinct from other locations of slow velocities where the transition from slow (~3 km/s) to fast (~5 km/s) velocities occurs over very narrow depth ranges (i.e., ~1 km; Figures 7c and 7d).

5. Interpretation

5.1. Velocity Interpretation

To constrain the thickness of sedimentary sequences from our smooth 3-D tomographic model, which does not have interfaces, we approximate the sediment/basement boundaries as velocity contours as discussed below (e.g., Moeller et al., 2013). It is necessary to constrain this interface from the refraction-derived velocity model because basement reflections are often ambiguous in seismic reflection profiles from both the SEGMeNT experiment and previous studies without the aid of other constraints (e.g., seismic velocity) and are completely absent in some parts of the rift, notably the accommodation zone and northern Central Basin (Figure 8b). Thus, seismic reflection data cannot be used to provide the comprehensive and consistent constraints on 3-D basin geometry provided by the 3-D velocity model presented here. Further, all of these seismic reflection data were acquired with short streamers (maximum length = 1,500 m) and thus can only constrain velocities up to ~1.5 km below the lake surface (water depth over Lake Malawi reaches 700 m in the Central Basin). Because of this limitation, the reflection data cannot be used alone to accurately estimate sediment thickness even in locations where basement is identified. Finally, seismic reflection data are not able to image prerift sediments beneath the synrift section from the most recent phase of extension. As a result, this study uses the refraction-derived seismic velocity model to constrain large-scale 3-D patterns in the thickness of synrift and prerift sediments, which cannot be accurately provided by any other data set.

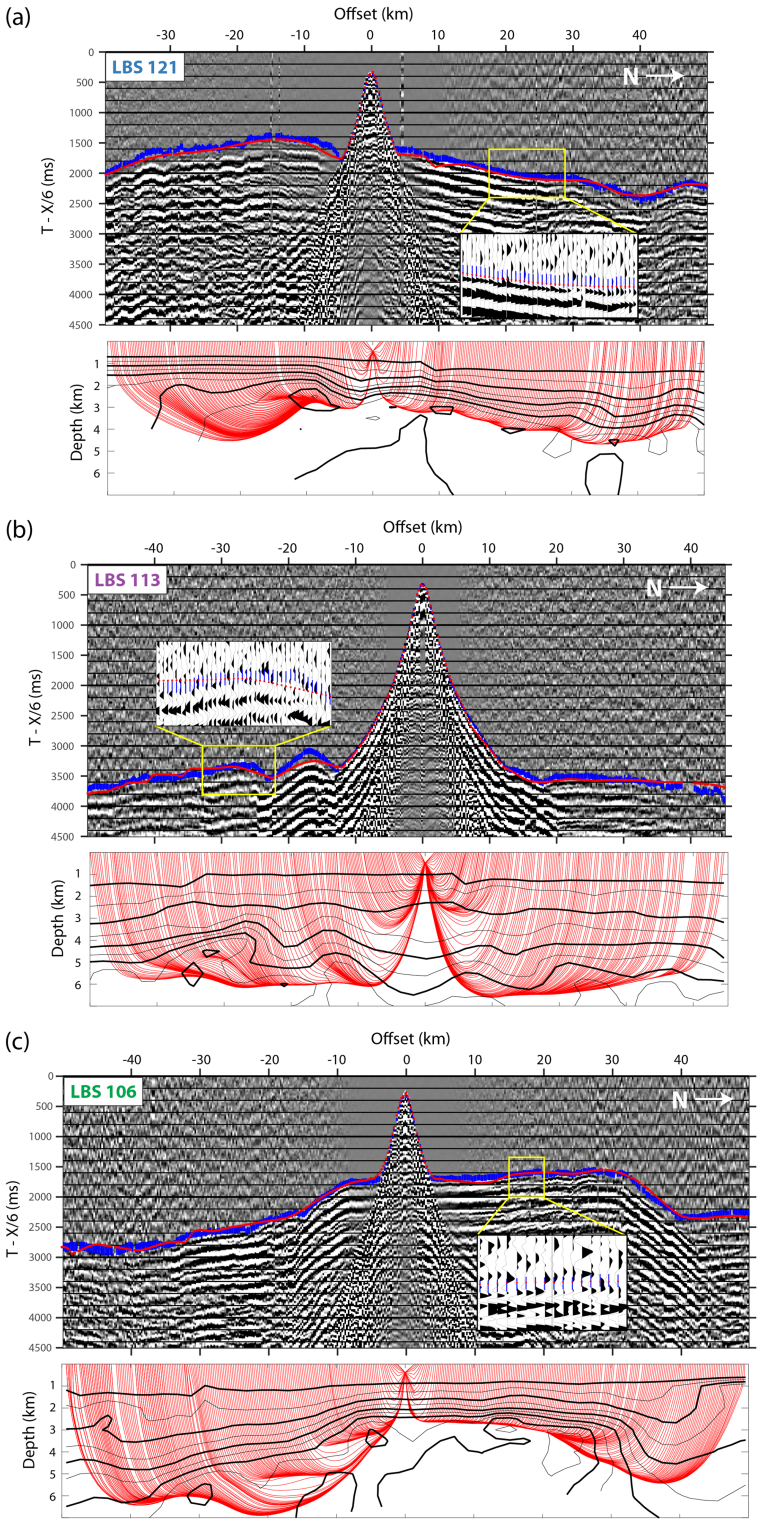

Figure 4. Examples of seismic receiver gathers (top) and predicted raypaths (bottom) for shots along the primary 2-D along-strike transect within the 3-D survey (for location of the profile see Figure 1c). The top plots show the record sections with observed picks in blue and predicted picks in red. The height of the observed pick indicates the observational error for each observation. Bottom plots show the predicted raypaths (red) for the shown picks against contours of the final velocity model (black lines). Instrument names are given in the top left of each record section and can be located within the study region by referencing Figure 1c. Zoom-ins are provided for each receiver gather, and the locations of the zoom-ins are shown by the yellow boxes. LBS = lake-bottom seismometers.

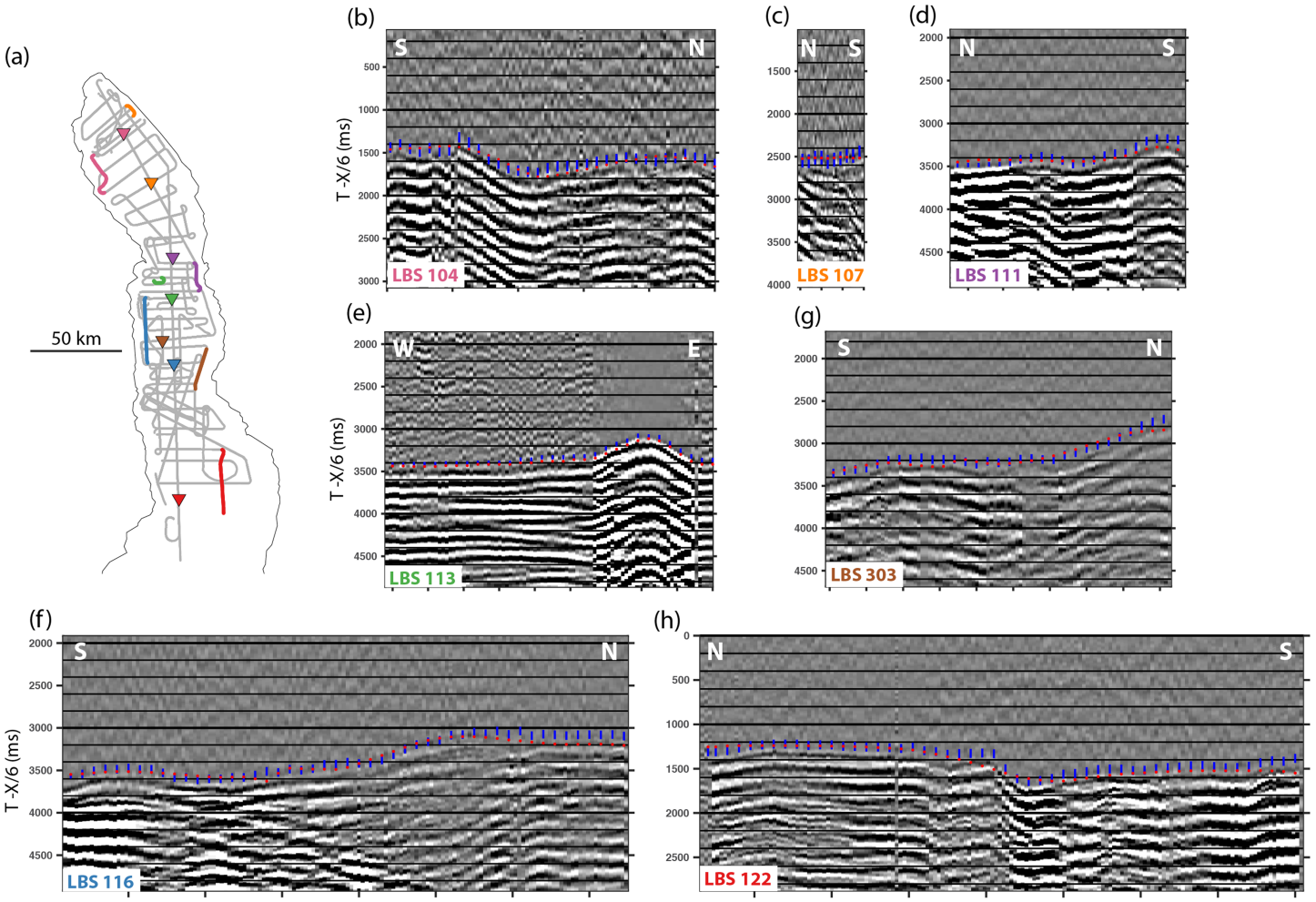

Figure 5. Examples of seismic record sections recorded along turns and lines of non-2-D geometry. The *x* axis is in terms of shot number and thus scales with the length of a given refraction line. The orientation of the line is shown by labels in the top right/left corners of each record. Observed picks are shown in blue where the height of the tick mark scales with observational error reported. Predicted picks are shown by the red points. To ensure ease of comparing the predicted/observed picks to the data only every fifth pick is marked. A map for instrument/line locations is shown in (a) where the color of the instrument matches the color of the line for which shots are shown. The background gray lines show the entire 3-D survey. Instrument numbers are labeled in the bottom left corner of each record section, and the color of the label matches the associated symbols in (a).

From both the LBS receiver gathers and the resulting velocity model, we identify three layers (not including the water) based on variations in velocity and velocity gradient. We interpret a ubiquitous shallow layer, with velocities gradually increasing from 1.5 to ~3.75 km/s, as a synrift sediment layer. These velocities are consistent with a normally compacting sedimentary section (progressive loss of pore space and subsequent increase in seismic velocity of sediments compacting under the weight of overlying sediments) as is observed in ocean basins and other rift systems (e.g., Hamilton, 1976; Moeller et al., 2013). Regions of the model with velocities of 1.5–3.75 km/s also correspond to synrift sediments where they are imaged in SEGMeNT seismic reflection profiles (Figure 8), although the thickness of the full sequence of synrift sediments cannot always be imaged or quantified by the seismic reflection data. Figure 9 shows a map of the depth to the base of this sedimentary sequence defined by the 3.75-km/s velocity contour.

In most of the study region, this sedimentary layer is directly underlain by a rapid increase to velocities of 5.5–6 km/s, consistent with upper crystalline crust (Christensen & Mooney, 1995). We choose a velocity contour of 4.5 km/s to approximate the top of crystalline basement, which lies within this high gradient zone. Over the majority of the basin, our choice of 4.5 km/s for the top of the crust matches a prominent, low-frequency reflection in SEGMeNT seismic reflection profiles from both the North and Central Basins where deep reflections are observed (Figures 8e and 8g). The only places where there are differences between the 4.5-km/s

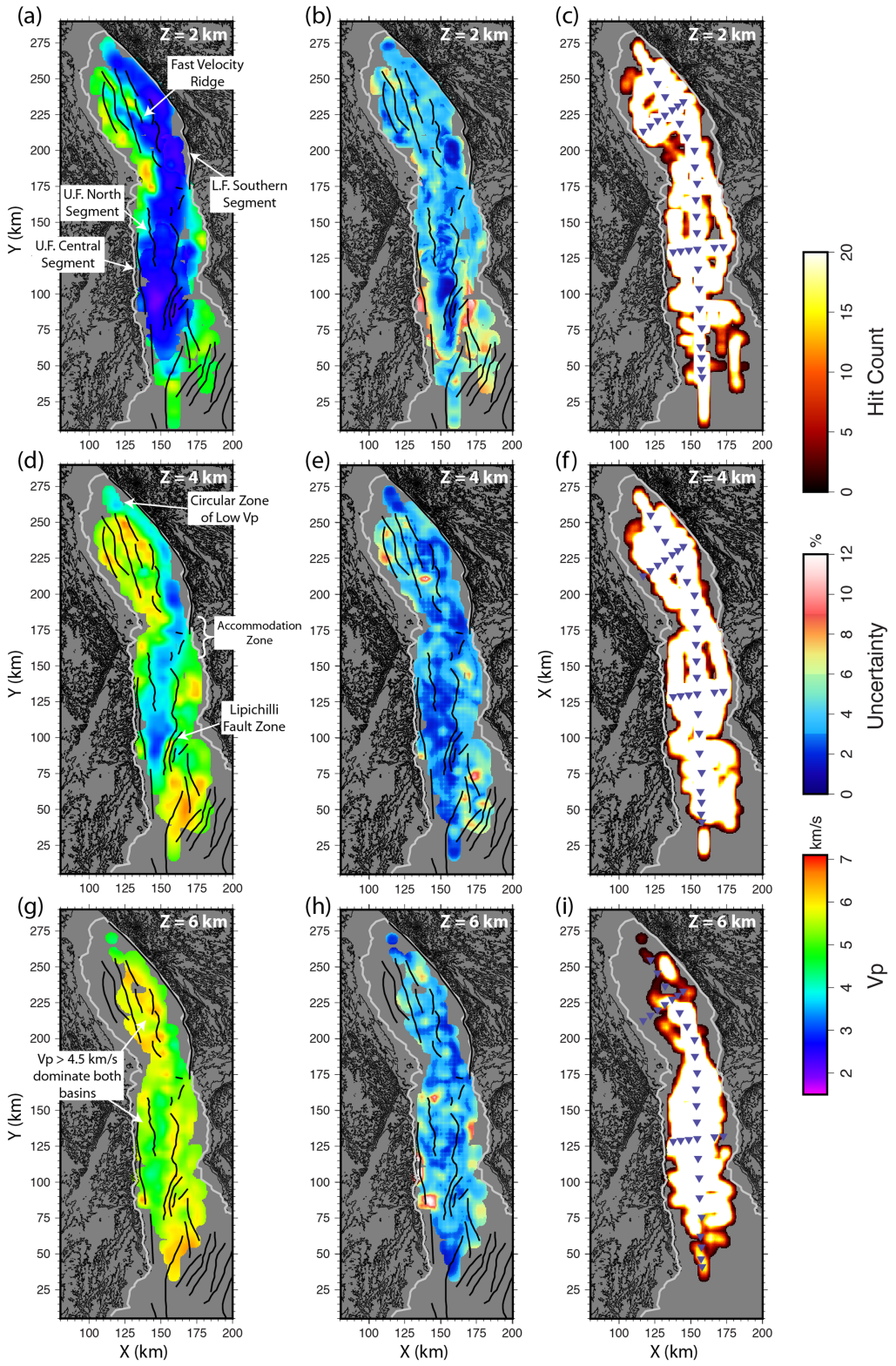

Figure 6. Depth slices through the final model in terms of *Vp* (a, d, and g), percent uncertainty (b, e, and h), and hit count (c, f, and i). Thick black lines indicate faults mapped in Mortimer et al. (2007), Lyons et al. (2011), and McCartney and Scholz (2016). The shoreline for Lake Malawi is shown by the light gray line in all plots. The locations of the instruments are shown by the blue triangles in the right column. Color scales stay constant along the columns. Note that the hit count maps use a color scale with a maximum value of 20 rays to allow easier viewing of low-ray coverage areas. Locations of interest are highlighted in (a), (d), and (g). U.F. = Usisya Fault; L.F. = Livingstone Fault.

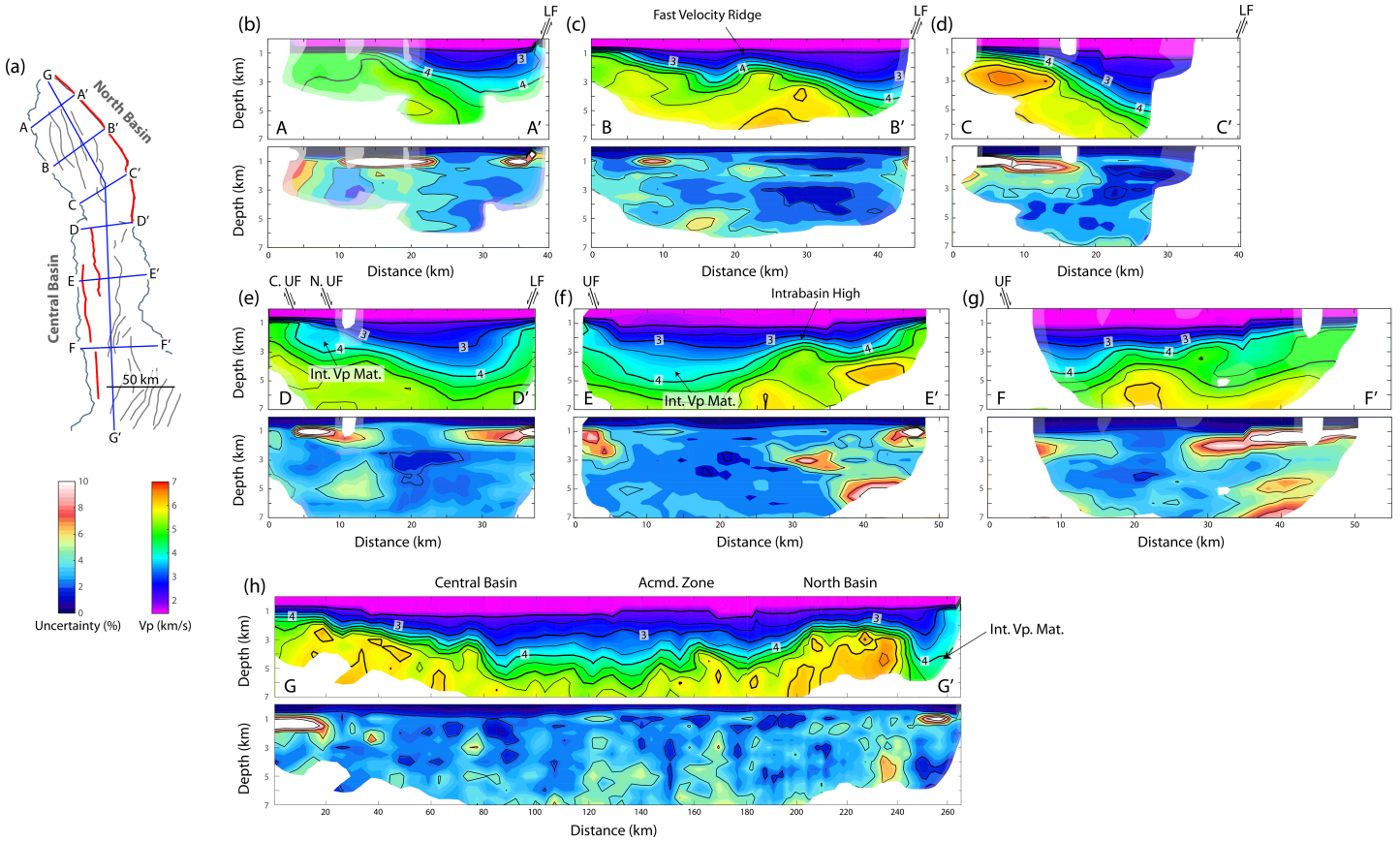

Figure 7. Cross-section slices through the final model in terms of velocity (top panels) and percent uncertainty (bottom panels). Locations of slices are shown on the map in (a) and are labeled on the individual cross sections. The locations of border faults (red) and intrabasin faults (gray) are shown in (a). All cross sections are shown going from west on the left to east on the right. Color scales are constant among all cross sections. The velocity cross sections are contoured with thick black lines labeling every 1 km/s and thin black lines every 0.5 km/s. Features of interest are marked on the cross sections. LF = Livingstone Fault; UF = Usisya Fault; C. = Central; N. = North; Int. Vp. Mat. = intermediate velocity material.

contour and the basement reflection in seismic reflection data are near the edges of the model where ray coverage is more limited. For example, near the border faults, the 4.5-km/s contour is sometimes locally shallower than the interpreted basement reflection in multi-channel seismic (MCS) data; thus, we consider our estimates of synrift sediment thickness, and fault throws derived from them, as conservative estimates. Where this low-frequency reflector is most clearly visible (for example, Figures 8e and 8g), our model contains a high-velocity gradient between the 3.75- and 4.5-km/s contours (e.g., they are separated by $<$0.5 s in TWTT). However, where this reflection is weak or absent, and imaging of the deep rift sediments is generally poor, as in the accommodation zone (Figure 8c), velocity gradients are lower, and the 3.75- and 4.5-km/s contours are separated by $>$1 s in TWTT.

In the accommodation zone, northern Central Basin and northernmost North Basin, a 2- to 4-km-thick layer is observed between the slower-velocity synrift sediments (1.5–3.75 km/s) and the crystalline basement ($>$4.5 km/s; Figure 7e). First-arriving refractions with apparent velocities of ~4 km/s are clearly observed on receiver gathers from several LBS in the Central Basin (Figure 4b; 113, 114, 115, 116, 117, 301, 302B, and 303) as well as instrument 103B in the northernmost North Basin. This interval has higher velocities and lower-velocity gradients than expected for compacting synrift sediments from the modern rift, making it distinct from velocities associated with sediments throughout much of the basin; accordingly, we interpret this intermediate velocity layer as sediment deposited during prior rifting episodes. This interpretation is consistent with the inference of preexisting sediment beneath the Malawi Rift based on outcrops onshore around the lake and locations where reflection imaging shows weak or absent acoustic basement.

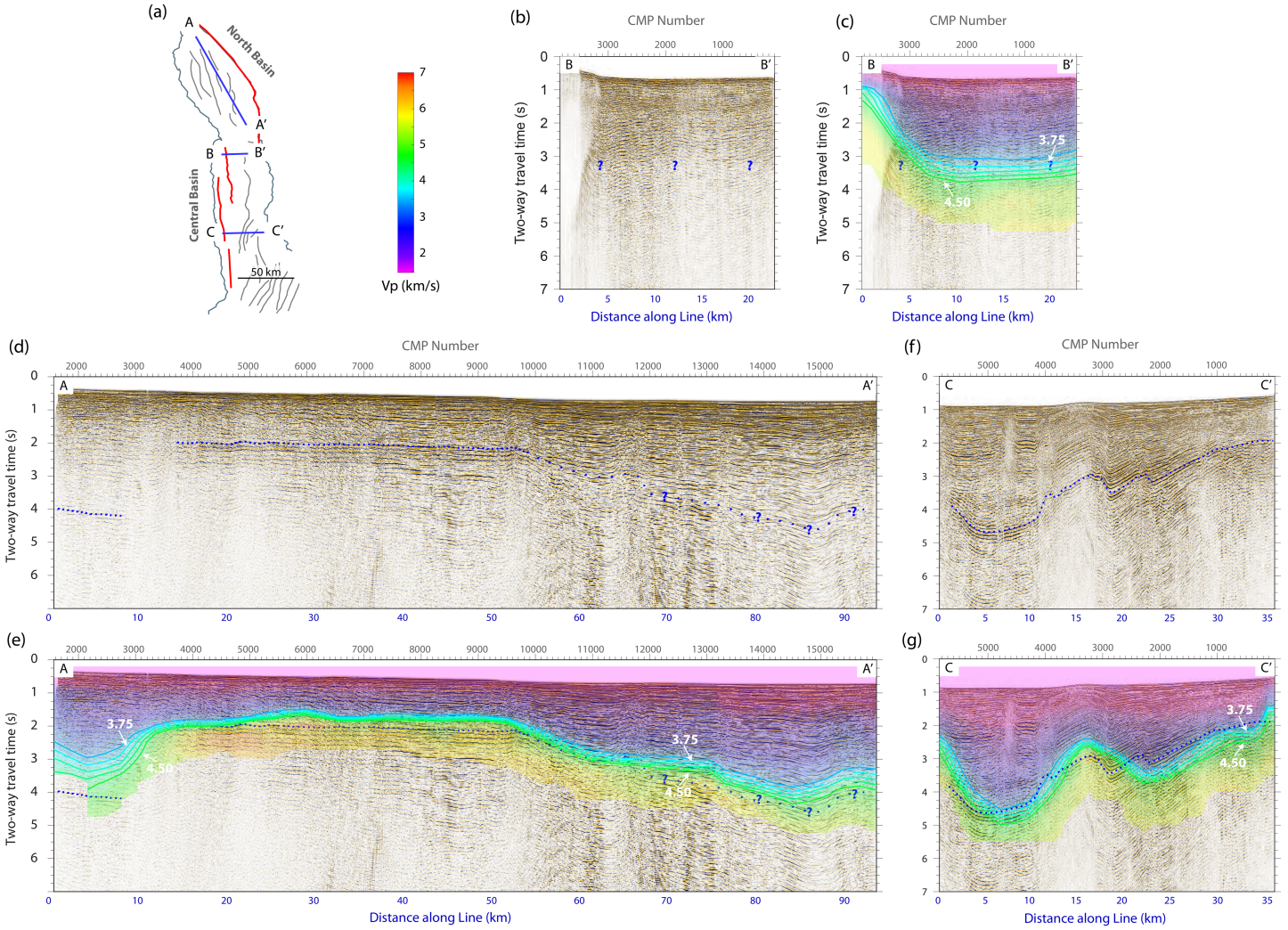

Figure 8. Comparison between time migrations of Study of Extension and maGmatism in Malawi and Tanzania MCS reflection lines and coincident 2-D profiles through the final velocity model in two-way travel time. The reflection lines are shown in (b), (c), and (d). On some profiles, a deep low-frequency reflection can be observed, which we interpret as representing the top of basement (dashed blue line). On other lines, basement is ambiguous (dotted blue line and question marks) or absent altogether (question marks). Even on profiles where a strong deep reflection is observed, the independent velocity model presented here greatly strengthened confidence in interpretations. The velocity model is plotted on top of the collocated reflection lines in (c), (e), and (g). Five velocity contours are shown as thick colored lines at 0.25 km/s intervals between 3.5 and 4.5 km/s. Locations of the profiles are shown in the inset map (a). The velocity color scale and spatial scale are the same for all profiles. The velocity model is masked where there is no ray coverage.

Crossley (1984) was one of the first to postulate that the Malawi Rift is underlain by preexisting sediment where it is crosscut by the Ruhuhu Basin and the Mwembeshi Shear Zone. Estimates of the thickness of this sedimentary package range from 1 km on the western shore in Malawi (Kemp, 1975) to ~3 km in the Ruhuhu Basin (Kreuser et al., 1990; Wopfner, 2002), suggesting that several kilometers of Karoo sequences may also be present beneath Lake Malawi. However, legacy reflection data were unable to image any Karoo sequences beneath the modern rift fill (Flannery & Rosendahl, 1990; Mortimer, Paton, et al., 2016).

Evidence for sediments deposited during prior rifting episodes is also documented north of Lake Malawi in the region between the Rukwa Rift and Lake Malawi. Karoo sediments and Cretaceous-Paleogene Red Sandstone Group sediments are widely distributed along the western side of the North Basin and RVP and continue northward into the Rukwa Rift (e.g., Jacobs et al., 1990; Roberts et al., 2010). These preexisting basins appear to strike subparallel to the trend of the North Basin, whereas the Ruhuhu Basin strikes nearly perpendicular to the trend of the Central Basin. Seismic reflection, borehole, and biostratigraphic data from the Rukwa Rift show that the Late-Pliocene-modern lake sediments are underlain by up to 10 km of

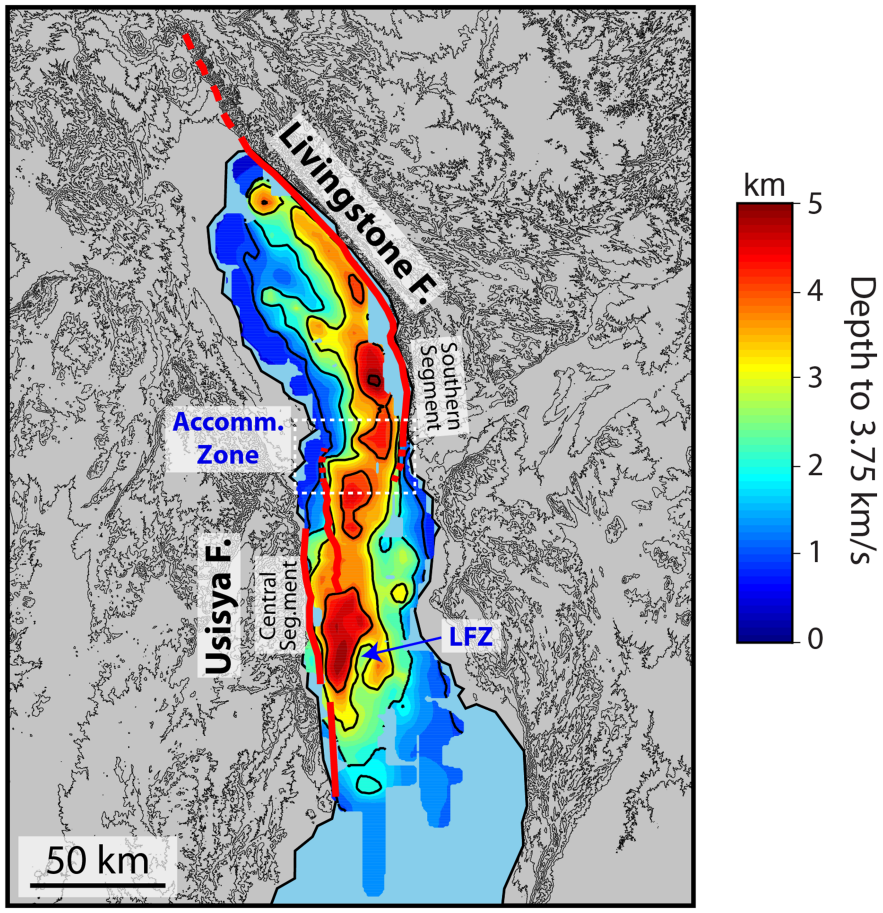

Figure 9. Depth to the base of synrift sediment defined by the 3.75-km/s velocity contour. Regions with no ray coverage are masked. Traces for the Livingstone and Usisya Faults are shown by the thick red lines (Lyons et al., 2011; McCartney & Scholz, 2016; Mortimer et al., 2007) and by dashed red lines where our refraction imaging indicates that the faults extend. The onshore extent of the Livingstone Fault is approximated by the dashed red line. Locations of interest are labeled including the accommodation zone between the two basins, the Lipichilli fault zone (LFZ), the southern segment of the Livingstone Fault, and the central segment of the Usisya Fault. Onshore elevation is shown at 200-m contour intervals.

Cretaceous to Paleogene Red Sandstone and Karoo sediments (Kilembe & Rosendahl, 1992; Peirce & Lipkov, 1988; Roberts et al., 2004, 2010; Wescott et al., 1991). Cretaceous- to Paleogene-age Red Sandstones also crop out along the northwestern side of the North Basin (e.g., Roberts et al., 2010). These onshore basins do not extend south past the northwest shore of the North Basin.

Although previous studies have hypothesized the presence of sediment associated with older extensional basins beneath Lake Malawi, no direct observations were previously available and the single drill core in the Central Basin reached a maximum depth of 380 m (Scholz et al., 2011), well within the synrift sediment package. We assert that sedimentary structures associated with older extension provides the most plausible interpretation for the intermediate velocity layers beneath the North and Central Basins. Figure 10 illustrates the thickness between the estimated base of synrift sediment and top of crystalline basement, which we interpret as sediment deposited during previous rifting episodes.

5.2. Estimating Cumulative Displacement Profiles for the Livingstone and Usisya Faults

Our 3-D velocity model provides unique constraints on 3-D patterns of synrift sediment thickness in a weakly extended rift. Together with constraints on footwall height from a 30-m digital elevation model from the Shuttle Radar Topography Mission (Farr et al., 2007), these estimates of synrift sediment thickness can be used to constrain variations in the throw of the border faults bounding the North and Central Basins.

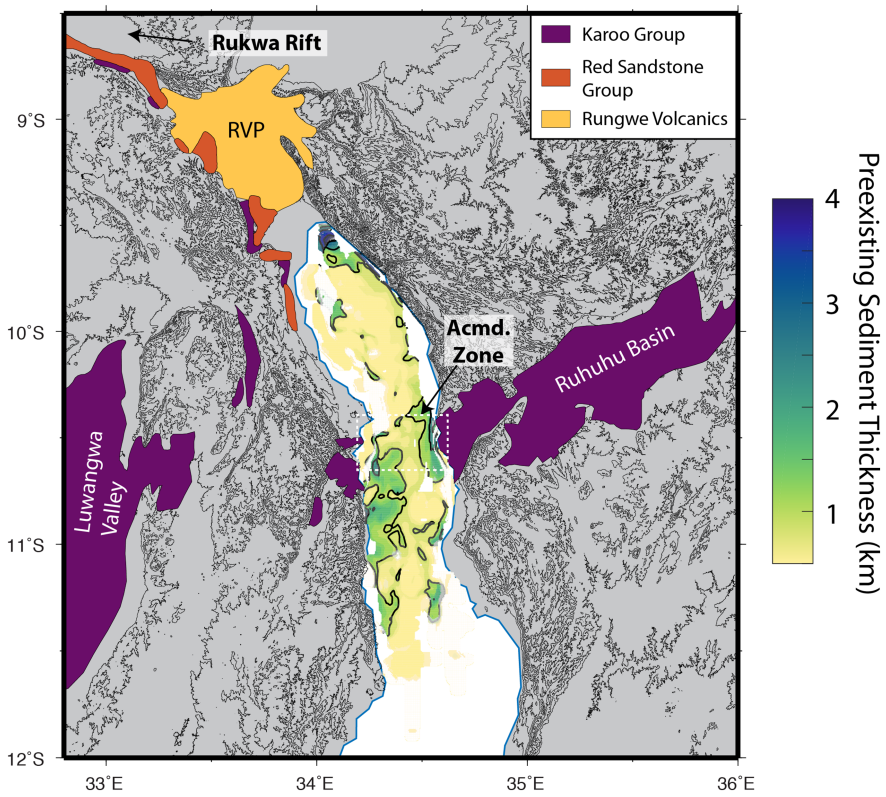

Figure 10. Map of thickness of sediments related to previous rifting episodes with simplified geologic map for comparison. Sediment thickness is contoured at 1-km intervals. Locations within the model with no ray coverage or velocity uncertainty >10% have been masked out. Geologic units were mapped following Bennett (1989), Delvaux (2001), Pinna et al. (2004), and Roberts et al. (2010). RVP = Rungwe Volcanic Province; Acmd Zone = accommodation zone.

Here we estimate cumulative vertical offset along the inferred lengths of the Livingstone and Usisya border faults. We calculate vertical offset along the border fault as the sum of the elevation of the footwall escarpment above lake level and the estimated depth to the base of synrift sediment below lake level. As this study is only concerned with cumulative vertical offset, we measure both footwall elevation and depth to the base of synrift sediment with respect to an arbitrary reference elevation—modern lake level. For more detailed analysis of the magnitude of footwall uplift compared to hanging wall downdrop, a calculation of a long-wavelength reference elevation would be needed. We do not calculate vertical offset for the onshore portion of the Livingstone Fault north of the lake due to a lack of sediment thickness constraints. To estimate footwall elevation, we extract profiles of elevation orthogonal to the strike of the border fault (the structural dip direction) from the Shuttle Radar Topography Mission following the procedure in Ellis and Barnes (2015). The maximum elevation for each dip profile is identified and then combined with all other measurements to create a strike profile along the border fault. We then adopt an iterative procedure to down-weight anomalously low elevations due to erosional features, such as river valleys (see the supporting information for details). Such erosional features suggest a reduction in the present-day elevation of the footwall, and thus, our estimates of footwall height represent a minimum. Our final elevation profile matches the overall shape of the original elevation profile well (Figure 11).

To estimate depth to the base of synrift sediment, we use the continuation of the same profiles (orthogonal to the strike of the border fault) into the lake and identify the maximum depth of the 3.75-km/s velocity contour, interpreted as the base of synrift sediments (see Figure S5). Locations with no ray coverage are excluded. Neither reflection nor refraction data were acquired close to the shorelines to minimize impacts on fishing activities close to shore, so sediment thickness immediately against the border fault is not constrained. Additionally, estimates of sediment thickness with low ray coverage near the edges of the velocity model are sometimes locally thinner than suggested by reflection data where basement can be imaged. For these reasons, our estimate of total throw represents a minimum. Total vertical offset is then estimated as the

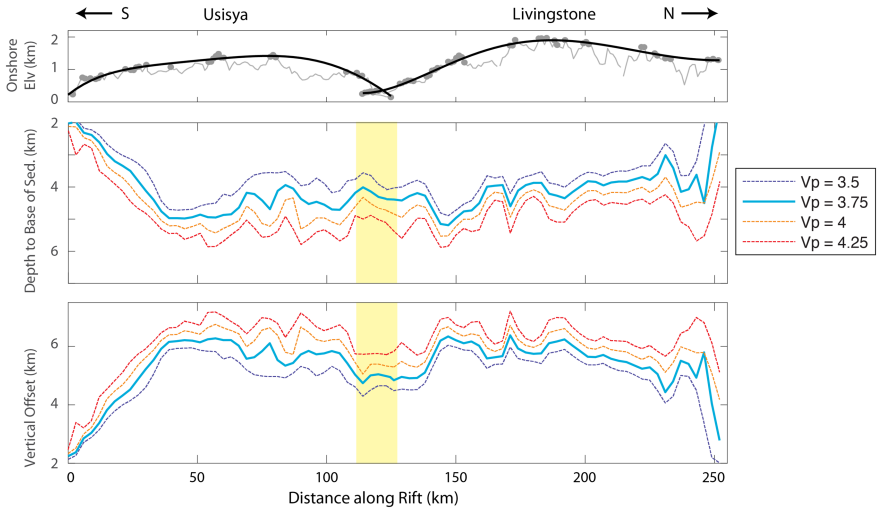

Figure 11. Profiles of elevation, depth to base of synrift sediments, and vertical offset for the Usisya (left, east dipping) and Livingstone (right, west dipping) faults plotted together. Profiles of elevation (top row) are taken along the footwall escarpment. The full elevation profile is shown as the thin gray line, the locations where elevation was taken for the final elevation profile are shown by the gray dots, and the final elevation profile is shown by the black line. Profiles of the depth to the base of synrift sediment (middle row) are shown for a range of velocities whereby the velocity defines the base of the sediment column. Profiles of total vertical offset (elevation above lake level + depth to the base of synrift sediment) are shown for the same range of velocity contours in the bottom row. Our preferred model is shown as the thick blue contour. The yellow rectangle shows the approximate region of fault overlap within the accommodation zone. The vertical scale on all three plots are consistent between each other.

sum of the elevation of the footwall escarpment and the depth to the base of synrift sediment beneath the lake, with maximum values of 6.3 ± 0.5 and 6.4 ± 0.4 km on the Usisya and Livingstone Faults, respectively. By assuming a dipping fault, we estimate fault throw from the vertical offset measurements. Previous reflection studies that were limited to the top few kilometers of the basins predict dip angles of 60°–70° for the Livingstone Fault (Wheeler & Rosendahl, 1994), and onshore measurements of fault dips are 60°–75° (Ebinger, 1989). Additionally, focal mechanisms from the Malawi Rift indicate that fault dips of ~60° continue to lower crustal depths in some parts of the Malawi Rift (Ekström et al., 2012; Jackson & Blenkinsop, 1993). Given fault dips between 75° and 60°, the fault throw would be between 6.5 and 7.3 km for the Usisya Fault and 6.6 and 7.4 km for the Livingstone Fault. Hereafter, we assume a dip of 60°.

Figure 11 shows estimated displacement profiles for the North and Central Basins. The Livingstone Fault measures ~140 km long with an additional ~30 km continuing onshore north of Lake Malawi and into the RVP, for a total length of 170 km. The Usisya border fault system measures ~140 km. Our estimated fault throw of 7.3 km for the Usisya Fault is higher than the 6.4 km reported by Contreras et al. (2000), estimated by using an average velocity of 2 km/s to convert from two-way travel time to depth in the absence of velocity constraints. Importantly, our analysis shows that more than two thirds of the total displacement accommodated on these faults sits below lake level, a result in contrast to the one-to-one ratio of displacement above and below lake level assumed by Contreras et al. (2000). However, the overall shape of the displacement profile is similar to Contreras et al. (2000).

6. Discussion

6.1. Fault Dimensions and Implications for Fault Lifespan

Our 3-D velocity model of synrift sediment distribution and estimated displacement profiles for the two faults provides insight into how strain is accommodated within and between the two basins. The large vertical offsets on the Usisya and Livingstone Faults (~6.3–6.4 km) confirm that these faults have facilitated a significant proportion of the total opening of the basins. For fault dips of between 60° and 75°, these faults have accommodated between ~3.6 and ~1.7 km of the total opening consistent with the 2.7–3.5 km of crustal extension estimated from previous studies (Ebinger, 1989). As described in

section 5.2, this is a minimum estimate. The dimensions of these faults are also consistent with relatively large elastic thickness estimated for this area (35–55 km, Ebinger et al., 1991; Pérez-Gussinyé et al., 2009); as shown by many previous studies, long faults form in regions of large T_e. Importantly, our imaging shows no indication for thickening of sediments against the proposed Mbamba Border Fault along the southeastern edge of the Central Basin (Figure 9), in agreement with McCartney et al. (2016). This result reinforces a fundamental similarity between the two basins in that both represent half-grabens with $>$7 km of fault throw on their solitary basin-bounding border fault.

Comparisons with the small number of available constraints on displacement for other large faults in strong lithosphere indicate that these fault throws are similar to those of other large normal faults of similar length. For comparison, other faults in the Western Rift with fault throw constraints (the Kivu-Rusizi Rift and Bunia Fault in the Albertine Rift) have lengths of ~100 and 75 km and fault throws of 2–5 and 5.3 km, respectively (Ebinger, 1989; Upcott et al., 1996). In the Baikal Rift, basin lengths are between 160 and 240 km, and synrift sediment deposits vary from 4 to 7.5 km (Hutchinson et al., 1992). While fault displacement has been broadly observed to scale with fault length (e.g., Dawers & Anders, 1995; Schlische et al., 1996), some faults reach large lengths with small throws consistent with the constant length model of fault growth. For example, the Kanda Fault in the Rukwa Rift is 160 km long and has a maximum fault scarp elevation of only ~45 m (Delvaux et al., 2012), and the Bilila-Mtakataka border fault in the southern Malawi Rift is ~100 km long and has only ~1 km of sedimentary strata (Jackson & Blenkinsop, 1997).

Long, large-offset faults such as those observed along the Western Rift are thought to form through the growth and linkage of smaller fault segments (e.g., Cartwright et al., 1995; Dawers & Anders, 1995), which results in a displacement profile in the shape of a flattened bell curve where displacement increases from 0 at the fault tips to a central maximum. The combined displacement profile for the two faults suggests that the Livingstone and Usisya Faults both broadly resemble this model (Figure 11). While both faults contain discrete segments, these segments are now thought to be presently linked in agreement with models of fault growth via segment linkage, though the timing of the linkage is debated (Contreras et al., 2000; Mortimer et al., 2016). Interestingly, the greatest displacement observed on the Livingstone Fault occurs along its southern segment (Figure 11), where water depth is greatest in the North Basin ($>$450 m, Figure 1b) and also where the fault is oriented approximately orthogonal to present-day extension direction (W-E; Saria et al., 2014).

Improved constraints on the dimensions of the Livingstone and Usisya Faults are also important for understanding whether the two faults continue to accommodate extension today. Several factors may control the maximum length and/or displacement that a fault can achieve. Numerous studies have shown that continued motion on a normal fault is favored by the difficulty in breaking a new fault but resisted by the need to overcome flexural restoring forces and the weight of the accumulated topography (e.g., Buck, 1993; Forsyth, 1992). Scholz and Contreras (1998) proposed an empirically constrained model for estimating maximum fault length/displacement in the context of rift systems. Utilizing a constant displacement-length scaling of ~0.03, and a modest value of T_e, this simple model predicts a maximum fault throw of ~5 km for the Usisya Fault. This value is smaller than the throw we observe (7.3 km).

Olive et al. (2014) propose an alternative theoretically based model, which suggests that surface processes of footwall erosion and hanging wall deposition may increase the life of a fault and hence its maximum achievable throw. Normal fault systems with a high rate of footwall uplift relative to erosion rate predict fault abandonment after relatively small total displacement, while systems with higher erosion rates relative to uplift can produce much greater total throw. The latter produces systems with a muted topographic change between the hanging and footwall, while the former retains a distinct topographic profile. For the Malawi Rift, the significant topographic profile suggests that erosion has been relatively slow compared to uplift rates, despite moderate present-day rainfall in the region ($>$1.5 m annually in some regions; Nicholson et al., 2013). With an estimated characteristic faulted layer thickness of ~30 km (Foster & Jackson, 1998), Olive et al. (2014) predict fault abandonment after only a few kilometers of displacement for the no-erosion end member. Their models with modest erosion such that significant relief is retained suggest maximum fault displacements of ~5 km prior to abandonment, again below our estimates of present-day fault throw. The large observed offsets on both the Livingstone and Usisya Faults compared to maximum offsets predicted by both empirical (Scholz & Contreras, 1998) and theoretical (Olive et al., 2014) studies imply that both faults are very close to, if not at, their maximum throw.

Importantly, both models discussed here are 2-D and make several simplifying assumptions like homogeneous sedimentary infill of the hanging wall, no preexisting topography or inherited structures, and no large-scale loads (i.e., volcanic centers), all of which are factors that may act to influence fault lifespan in our study region. Nevertheless, our observations of significant offset suggest that Livingstone and Usisya Faults are likely near or at their maximum size suggesting that a migration of strain inward onto presently active intrabasin structures may be imminent or occurring.

6.2. Accommodation Zone Structure and Implications for Models of Fault Growth

Our velocity models also provide new constraints on accommodation zone structure and the growth of the Livingstone and Usisya Faults. In the accommodation zone, we estimate a 4.3-km-thick package of synrift sediment, which smoothly shifts from an eastward thickening section within the North Basin to a westward thickening section in the Central Basin (Figures 9 and 11). Footwall elevation on either side of the accommodation zone is modest where the Ruhuhu River enters Lake Malawi to the east and the S. Rukuru River enters to the west. Cross sections across the accommodation zone reveal a nearly symmetric basin, suggesting that the border faults overlap and both faults influence this region (Figures 6d and 7e), which is not possible to discern from onshore elevation alone. Synrift sediment thicken both to the west and the east in our velocity model over a 20-km-long sector along the rift (i.e., Figures 6a and 6d), which we interpret as the area of overlapping influence of the two border faults.

Our observations are broadly consistent with imaging of the accommodation zone by Project PROBE (Scholz, 1989), which show it to be a broad low relief feature (Specht & Rosendahl, 1989) similar to accommodation zones observed in other parts of the Western Rift (Rosendahl, 1987); however, PROBE data did not clearly image the base of synrift sediment in the accommodation zone. A small topographic high is also interpreted within this broad low relief zone (Specht & Rosendahl, 1989), which Flannery and Rosendahl (1990) attributed in part to the intersection with the Ruhuhu Basin. We do not observe any positive relief feature within this zone in our velocity model, but it may be too small to resolve with our study.

Analogue clay models and previous field studies suggest that in regions of fault tip overlap, accommodation zones tend to be narrow and strike nearly parallel to the trend of the basins (e.g., Faulds & Varga, 1998; Morley et al., 1990; Paul & Mitra, 2013). Where no overlap exists, accommodation zones are wide and strike parallel to the extension direction. Our imaging shows that the accommodation zone strikes nearly parallel to the trend of the basins and is ~20 km wide (Figure 6d), consistent with predictions, and yielding a broad depositional apron between the two depocenters (e.g., Scholz, 1995b). We conclude that significant fault tip overlap exists at the accommodation zone between the Livingstone and Usisya Faults and the combined motion on these faults results in deep, continuous sediment infill between the two basins.

In the region of fault tip overlap, our profiles of displacement show a thick sedimentary section (~4.3 km) and relatively large vertical throw (~4.5 km). We hypothesize that the southern end of the Livingstone Fault and northern end of the Usisya Fault must have been active in the region from a very early stage to generate this much vertical offset at their intersection. Using reflection imaging, Morley (1999) showed that many basins within the EARS achieved their fault length early leading to nearly stationary locations of fault tips for most of the lifespan of the basins. Within the Central Basin, McCartney and Scholz (2016) similarly found that intrabasinal faults established their length rapidly through the linkage of fault segments. These observations match predictions from the constant-length model, whereby fault length is established rapidly and varies little afterward, allowing displacement to accrue through time (e.g., Curry et al., 2016; Morley, 2002; Nicol et al., 2005; Walsh et al., 2002). In detail, the thermochronological study of the Livingstone Fault by Mortimer, Kirstein, et al. (2016) found that some segments may not have linked until very recently (~1.6 Ma), and the stratigraphic analysis of Contreras et al. (2000) on the Usisya Fault argued for alternating periods of increasing fault length and/or fault displacement on some smaller-scale segments. At the full basin scale, our observation of significant displacement across the overlapping fault tips of the Livingstone and Usisya Faults signifies the early establishment of their overall respective fault lengths.

6.3. Influences on Basin Structure and the Role of Preexisting Features

Nearly every aspect of the rifting process is thought to be influenced by preexisting structures, from rift initiation through to plate rupture. However, obtaining direct constraints on the relationship between remnant structures and rift evolution is challenging as recent extensional processes often overprint remnant

structures. Our 3-D velocity model of the Malawi Rift provides unique new constraints on influential preexisting features beneath this early stage rift, in particular the distribution and character of prerift sediments and basin structure. As introduced in section 5.1, Late Paleozoic Karoo-age and Cretaceous basins are observed onshore, and our velocity model reveals associated thick packages of interpreted preexisting sediment in both the North and Central Basins (Figure 10).

In the northern Central Basin and accommodation zone, prerift sediments are estimated to have an average thickness of ~1.5–2.5 km covering an area of ~250 km^2 and likely reflect the offshore continuation of the Karoo-age Ruhuhu Basin. Within the North Basin, estimated preexisting sediments are much more spatially limited (localized within the northernmost part of the basin) but, where they exist, they are much thicker (up to 4.6 km; Figure 10). Seismic reflection data and LBS receiver gathers show that the southern edge of this North Basin feature is sharp (Figures 8d and 8e). The presence of a thick package of preexisting sediment in the northernmost North Basin likely reflects the offshore continuation of one or both Cretaceous to Paleogene Red Sandstone and Karoo-age basins, which are preserved onshore along the northwestern edge of the North Basin and north into the Rukwa Rift (Kilembe & Rosendahl, 1992; Peirce & Lipkov, 1988; Roberts et al., 2004, 2010), and these rocks outcrop along the northwestern edge of the North Basin (Figure 10). The observation of preexisting sediment in the northernmost part of the North Basin expands on evidence for prior rifting-related sediments onshore (e.g., Jacobs et al., 1990; Roberts et al., 2010), and is consistent with predictions from balanced stratigraphic cross sections (Ebinger et al., 1989). We suggest that this preexisting material represents the remnants of larger extensional basins that continue from the Rukwa Rift into the northern North Basin (Figure 10). These prior rifting-related packages of sediment mapped by this study are further evidence of a long-lived corridor of intermittent extension along the Tanganyika-Rukwa-Malawi segment of the EARS (Delvaux, 1991, 2001) active over multiple rift phases since the Late Paleozoic.

These preexisting structures appear to influence the development of intrabasin and basin structure in both the North and Central basins (Mortimer et al., 2007; Mortimer, Paton, et al., 2016; Wheeler & Karson, 1989) and the accommodation zone between them. We highlight the correlation between the relatively simple intrabasinal faulting of the North Basin and the limited extent of prior rifting-related material there (~5% of the basin) compared to the complex faulting within the Central Basin and the broad extent of prior rifting-related material there (~25% of the basin). These observations support the argument of Mortimer, Paton, et al. (2016) that the increased complexity of structure within the Central Basin is due to the presence of Karoo-age preexisting structures that crosscut the basin. However, McCartney and Scholz (2016) instead suggest that complex intrabasinal faulting may have been primarily influenced by the underlying Proterozoic basement fabric, similar to what others have observed in different rift settings (e.g., Gulf of Corinth; Nixon et al., 2016). The variation in intrabasinal complexity between the Central and North basins likely results from a combination of factors, including the presence of inherited Karoo-age to Cretaceous/Paleogene structures mapped in this study.

Large-scale preexisting structures, like basins and shear zones, likely also influence how extension is accommodated during the rifting process and specifically restrict or promote border fault growth (e.g., Manighetti et al., 2001). Many authors highlight the marked parallelism between the trend of the Livingstone Fault and the underlying Ubendian basement foliations (e.g., Ebinger et al., 1999; Morley, 2010; Mortimer et al., 2007; Ring, 1994; Wheeler & Karson, 1989; Figure 1b), which may reflect the rapid establishment of the 170-km-long fault trace along preexisting zones of weakness (e.g., Corti et al., 2013; Morley, 2010; Reeve et al., 2015). In contrast, there is no clear relationship between inherited faults/foliations and synrift structure beneath the 140-km-long Usisya Fault, where the underlying basement rock is characterized by more moderately dipping foliations with no single preferred orientation (Fritz et al., 2009; Theunissen et al., 1996). Additionally, the Central Basin is bound to the south by the Karoo-aged Maniamba Trough and to the north by the Karoo-aged Ruhuhu Basin (Catuneanu et al., 2005; Ebinger et al., 1987), both of which obliquely cross the Malawi Rift. Versfelt and Rosendahl (1989) postulated that intersection of the Ruhuhu Basin with the Malawi Rift may have influenced the opposing polarity of the Usisya and Livingstone Faults given that structures associated with the Ruhuhu Basin are likely oriented nearly orthogonal to the Central Basin. Our study demonstrates that these structures continue offshore across Lake Malawi at the accommodation zone and the northern termination of the Usisya Fault (Figure 10). The presence of preexisting structural obstacles can act to inhibit the propagation of a fault but may not influence the accumulation of slip on the fault leading to shorter faults with large throws (e.g., Manighetti et al., 2001). The presence of prominent crossing structures (the

Maniamba Trough and Ruhuhu Basin) at the north and south ends of the Usisya Fault may have been one factor that ultimately restricted its growth leading to a shorter fault trace but similar amount of throw compared to the Livingstone Fault. The constraints from this study on fault throw and the presence of preexisting structures in Lake Malawi adds much needed observations to inform the debate surrounding the role of preexisting structures in the rifing process.

7. Conclusions

We use seismic refraction data acquired by LBS to create a 3-D *P* wave velocity model of the northern basins of the Malawi Rift. This model provides new, unique constraints on basin and upper crustal structure in a weakly extended rift that can be used to understand normal fault growth, the formation and evolution of accommodation zones, and the role of preexisting structures on rift development. These results will provide a foundation for future, more detailed studies utilizing the collocated SEGMeNT seismic reflection data. Our velocity model shows that ~4.3 km of sediment exists in the accommodation zone between these opposite-polarity border faults, which smoothly shifts from eastward-thickening sediments within the North Basin to the westward-thickening sediments in the Central Basin. This observation matches predictions of analogue models for overlapping border faults of opposite polarity. The significant thickness of sediment within the accommodation zones indicates that both faults likely reached their lengths early, consistent with the constant-length model of fault growth. We present new constraints on total offset on the Livingstone and Usisya Faults and find that both faults have accumulated vertical offsets of 6.3–6.4 km (7.3–7.4 km of fault throw assuming a fault dip of 60°). The significant displacement accommodated on both faults indicates that the faults are likely near their maximum dimensions, and this may suggest that an inward migration of strain away from the boarder faults may be imminent. Thick packages of preexisting sediment interpreted in both basins are thought to be associated with outcropping Late Paleozoic Karoo and Cretaceous-Paleogene basins onshore. These previously active extensional basins may have influenced the development of the complex structure of the two basins, with the limited extent of prior rifting-related sediment in the North Basin potentially facilitating development of comparatively simple intrabasinal faulting compared to the more complex Central Basin. We correlate the significant package of preexisting sediment at the northernmost end of the North Basin with Cretaceous and Karoo-age basins that continue NW to the Rukwa Rift system. This observation adds further evidence that the region between the Rukwa and Malawi Rifts has been a corridor of extension for a significant period of time.

Acknowledgments

The authors gratefully acknowledge all of those involved in the successful acquisition of this large and complex experiment. Acquisition of this data set would not have been possible without the support from communities in our study area, national and regional governmental entities in Malawi and Tanzania, and administrative and technical support from institutes, companies, and geological surveys in the United States, Malawi, Tanzania, Denmark, and Canada. We gratefully acknowledge the captains and crews of the *Katundu*, *Ndunduma*, and *Chilembwe* and the entire science party that helped to acquire this data set. Instruments were provided by the Ocean Bottom Seismology Instrumentation Program (OBSIP) from the Scripps Institute of Oceanography (SIO). We particularly acknowledge Jeff Babcock, Ernest Aaron, Mark Gibaud, Martin Ripa, and others at the SIO Institutional Instrument Contributor. We gratefully acknowledge Per Trinhammer from Aarhus University and Jack Schelling for their incredible help with seismic source operations. We also thank Jacob Greenberg for his help with onboard ship operations. We thank Cynthia Ebinger and Jean-Arthur Olive for very useful discussions regarding this work. Seismic data used in this study are available through the Incorporated Research Institutions for Seismology Data Management Center (http://ds.iris.edu/ds/nodes/dmc/), network code YQ. Data were processed using Seismic Unix maintained by John Stockwell (http://www.cwp.mines.edu/cwpcodes/) and picked using OpendTect (https://www.opendtect.org/). This research was supported by National Science Foundation (NSF) grant EAR-1110921, Lamont-Doherty Earth Observatory, and the NSF Graduate Student Research Fellowship Program. We also thank Lindsay Worthington, Jolante van Wijk, Uri Ten Brink, and an anonymous reviewer for insightful reviews that strengthened this manuscript.

References

Bennett, J. D. (1989). Review of Lower Karoo coal basins and coal resource development in parts of central and southern Africa with particular reference to northern Malawi (No. WC/89/21). Keyworth: British Geological Survey.

Buck, W. R. (1993). Effect of lithospheric thickness on the formation of high- and low-angle normal faults. *Geology*, *21*, 933–936.

Cartwright, J. A., Trudgill, B. D., & Mansfield, C. S. (1995). Fault growth by segment linkage: An explanation for scatter in maximum displacement and trace length data from the Canyonlands Grabens of SE Utah. *Journal of Structural Geology*, *17*(4), 1319–1326.

Catuneanu, O., Wopfner, H., Eriksson, P. G., Cairncross, B., Rubidge, B. S., Smith, R. M. H., & Hancox, P. J. (2005). The Karoo basins of south-central Africa. *Journal of African Earth Sciences*, *43*(1-3), 211–253. https://doi.org/10.1016/j.jafrearsci.2005.07.007

Christensen, N. I., & Mooney, W. D. (1995). Seismic velocity structure and composition of the continental crust: A global view. *Journal of Geophysical Research*, *100*(B7), 9761–9788. https://doi.org/10.1029/95JB00259

Contreras, J., Anders, M. H., & Scholz, C. H. (2000). Growth of a normal fault system: Observations from the Lake Malawi basin of the east African rift. *Journal of Structural Geology*, *22*, 159–168.

Corti, G., Ranalli, G., Agostini, A., & Sokoutis, D. (2013). Inward migration of faulting during continental rifting: Effects of pre-existing lithospheric structure and extension rate. *Tectonophysics*, *594*(C), 137–148. https://doi.org/10.1016/j.tecto.2013.03.028

Corti, G., van Wijk, J., Cloetingh, S., & Morley, C. K. (2007). Tectonic inheritance and continental rift architecture: Numerical and analogue models of the East African Rift system. *Tectonics*, *26*, TC6006. https://doi.org/10.1029/2006TC002086

Cowie, P. A., & Scholz, C. H. (1992). Displacement-length scaling relationship for faults: Data synthesis and discussion. *Journal of Structural Geology*, *14*(10), 1149–1156.

Crossley, R. (1984). Controls of sedimentation in the Malawi Rift valley, Central Africa. *Sedimentary Geology*, *40*, 33–50.

Curry, M. A. E., Barnes, J. B., & Colgan, J. P. (2016). Testing fault growth models with low-temperature thermochronology in the northwest Basin and Range, USA. *Tectonics*, *35*, 2467–2492. https://doi.org/10.1002/(ISSN)1944-9194

Daly, M. C., Chorowicz, J., & Fairhead, J. D. (1989). Rift basin evolution in Africa: The influence of reactivated steep basement shear zones. In M. A. Cooper & G. D. Williams (Eds.), *Inversion tectonics: Geological Society Special Publications No. 44* (pp. 309–334). Oxford, UK: The Geological Society. https://doi.org/10.1144/GSL.SP.1989.044.01.17

Dawers, N. H., & Anders, M. H. (1995). Displacement-length scaling and fault linkage. *Journal of Structural Geology*, *17*(5), 607–614.

Dawers, N. H., Anders, M. H., & Scholz, C. H. (1993). Growth of normal faults: Displacement-length scaling. *Geology*, *21*, 1107–1110.

Delescluse, M., Funck, T., Dehler, S., Louden, K. E., & Watremez, L. (2015). The oceanic crustal structure at the extinct, slow to ultraslow Labrador Sea spreading center. *Journal of Geophysical Research: Solid Earth*, *120*, 5249–5272. https://doi.org/10.1002/(ISSN)2169-9356

Delvaux, D. (1991). The Karoo to recent rifting in the Western Branch of the East African Rift System: A bibliogrpahical synthesis. *Royal Museum of Central Africa - Annual Report, 1989-1990*, 63–83.

Delvaux, D. (2001). Tectonic and palaeostress evolution of the Tanganyiika-Rukwa-Malawi rift segment, East African Rift System. In P. A. Ziegler, A. H. F. Robertson, & S. Crasquin-Soleau (Eds.), *Peri-Tethyan Rift/Wrench Basins and passive margins* (Vol. 186, pp. 545–567). Paris: Mémoires du Muséum National d'Histoire Naturelle.

Delvaux, D., Kervyn, F., Macheyeki, A. S., & Temu, E. B. (2012). Geodynamic significance of the TRM segment in the East African Rift (W-Tanzania): Active tectonics and paleostress in the Ufipa plateau and Rukwa basin. *Journal of Structural Geology*, *37*(C), 161–180. http://doi.org/10.1016/j.jsg.2012.01.008

Ebinger, C., Poudjom, D., Mbede, E., Foster, A., & Dawson, J. B. (1997). Rifting Archaean lithosphere: The Eyasi–Manyara–Natron rifts, East Africa. *Journal of the Geological Society of London*, *154*, 947–960.

Ebinger, C. J. (1989). Geometric and kinematic development of border faults and accomodation zones, Kivu-Rusizi Rift, Africa. *Tectonics*, *8*(1), 117–133. https://doi.org/10.1029/TC008i001p00117

Ebinger, C. J., & Casey, M. (2001). Continental breakup in magmatic provinces: An Ethiopian example. *Geology*, *29*(6), 527–525.

Ebinger, C. J., Deino, A. L., Drake, E., & Tesha, A. L. (1989). Chronology of volcanism and rift basin propagation: Rungwe Volcanic Province, East Africa. *Journal of Geophysical Research*, *94*, 15,785–15,803. https://doi.org/10.1029/JB094iB11p15785

Ebinger, C. J., Deino, A. L., Tesha, A. L., Becker, T., & Ring, U. (1993). Tectonic controls on rift basin morphology: Evolution of the northern Malawi (Nyasa) Rift. *Journal of Geophysical Research*, *98*, 17,821–17,836. https://doi.org/10.1029/93JB01392

Ebinger, C. J., Jackson, J. A., Foster, A. N., & Hayward, N. J. (1999). Extensional basin geometry and the elastic lithosphere. *Philosophical Transactions of the Royal Society A: Mathematical, Physical and Engineering Sciences*, *357*, 741–765.

Ebinger, C. J., Karner, G. D., & Weissel, J. K. (1991). Mechanical strength of extended continental lithosphere—Constraints from the western rift system, East Africa. *Tectonics*, *10*(6), 1239–1256. https://doi.org/10.1029/91TC00579

Ebinger, C. J., Rosendahl, B. R., & Reynolds, D. J. (1987). Tectonic model of the Malawi rift, Africa. *Tectonophysics*, *141*(1-3), 215–235.

Ebinger, C. J., & Scholz, C. A. (2012). Continental rift basins: The East Africa perspective. In C. Busby & A. Azor (Eds.), *Tectonics of sedimentary basins recent advances* (pp. 185–208). Chichester, UK: John Wiley.

Ekström, G., Dziewoński, A. M., & Nettles, M. (2012). The global CMT project 2004-2010: Centroid-moment tensors for 13,017 earthquakes. *Physics of the Earth and Planetary Interiors*, *200-201*(C), 1–9. https://doi.org/10.1016/j.pepi.2012.04.002

Ellis, M. A., & Barnes, J. B. (2015). A global perspective on the topographic response to fault growth. *Geosphere*, *11*(4), 1008–1023. https://doi.org/10.1130/GES01156.1

Fagereng, Å. (2013). Fault segmentation, deep rift earthquakes and crustal rheology: Insights from the 2009 Karonga sequence and seismicity in the Rukwa–Malawi rift zone. *Tectonophysics*, *601*(C), 216–225. https://doi.org/10.1016/j.tecto.2013.05.012

Farr, T. G., Rosen, P. A., Caro, E., Crippen, R., Duren, R., Hensley, S., et al. (2007). The Shuttle Radar Topography Mission. *Reviews of Geophysics*, *45*, RG2004. https://doi.org/10.1029/2005RG000183

Faulds, J. E., & Varga, R. J. (1998). The role of accommodation zones and transfer zones in the regional segmentation of extended terranes. *Geological Society of America Special Papers*, *323*, 1–45. https://doi.org/10.1130/0-8137-2323-X.1

Flannery, J. W., & Rosendahl, B. R. (1990). The seismic stratigraphy of Lake Malawi, Africa: Implications for interpreting geological processes in lacustrine rifts. *Journal of African Earth Sciences (and the Middle East)*, *10*(3), 519–548. https://doi.org/10.1016/0899-5362(90)90104-M

Forsyth, D. W. (1992). Finite extension and low-angle normal faulting. *Geology*, *20*, 27–30.

Foster, A. N., & Jackson, J. A. (1998). Source parameters of large African earthquakes: Implications for crustal rheology and regional kinematics. *Geophysical Journal International*, *134*, 422–448.

Fritz, H., Abdesalam, M., Ali, K. A., Bingen, B., Collins, A. S., Fowler, A. R., et al. (2013). Orogen styles in the East African Orogen: A review of the Neoproterozoic to Cambrian tectonic evolution. *Journal of African Earth Sciences*, *86*(C), 65–106. https://doi.org/10.1016/j.jafrearsci.2013.06.004

Fritz, H., Tenczer, V., Hauzenberger, C., Wallbrecher, E., & Muhongo, S. (2009). Hot granulite nappes—Tectonic styles and thermal evolution of the Proterozoic granulite belts in East Africa. *Tectonophysics*, *477*(3-4), 160–173. https://doi.org/10.1016/j.tecto.2009.01.021

Furman, T. (2007). Geochemistry of East African Rift basalts: An overview. *Journal of African Earth Sciences*, *48*(2-3), 147–160. https://doi.org/10.1016/j.jafrearsci.2006.06.009

Goldsworthy, M., & Jackson, J. (2001). Migration of activity within normal fault systems: Examples from the Quaternary of mainland Greece. *Journal of Structural Geology*, *23*, 489–506.

Hamilton, E. L. (1976). Variations of density and porosity with depth in deep-sea sediments. *Journal of Sedimentary Petrology*, *46*(2), 280–300.

Hanson, R. E. (2003). Proterozoic geochronology and tectonic evolution of southern Africa. In M. Yoshida, B. F. Windley, & S. Dasgupta (Eds.), *Proterozoic East Gondwana supercontinent assembly and breakup* (pp. 427–463). London: Geological Society.

Hayward, N. J., & Ebinger, C. J. (1996). Variations in the along-axis segmentation of the Afar Rift system. *Tectonics*, *15*, 244–257. https://doi.org/10.1029/95TC02292

Hutchinson, D. R., Golmshtok, A. J., Zonenshain, L. P., Moore, T. C., Scholz, C. A., & Klitgord, K. D. (1992). Depositional and tectonic framework of the rift basins of Lake Baikal from multichannel seismic data. *Geology*, *20*, 589–592.

Jackson, C. A. L., Bell, R. E., Rotevatn, A., & Tvedt, A. B. M. (2017). Techniques to determine the kinematics of synsedimentary normal faults and implications for fault growth models. *Geological Society, London, Special Publications*, *SP439*, 22–31. https://doi.org/10.1144/SP439.22

Jackson, J., & Blenkinsop, T. (1993). The Malawi Earthquake of March 10, 1989: Deep Faulting within the East African Rift system. *Tectonics*, *12*(5), 1131–1139. https://doi.org/10.1029/93TC01064

Jackson, J., & Blenkinsop, T. (1997). The Bilila-Mtakataka fault in Malawi: An active, 100-km long, normal fault segment in thick seismogenic crust. *Tectonics*, *16*, 137–150. https://doi.org/10.1029/96TC02494

Jacobs, L. L., Winkler, D. A., Kaufulu, Z. M., & Downs, W. R. (1990). The dinosaur beds of Northern Malawi, Africa. *National Geographic Research*, *6*(2), 196–204.

Kemp, J. (1975). *The geology of the Uzumara area*. South Africa: Government Printer.

Kilembe, E. A., & Rosendahl, B. R. (1992). Structure and stratigraphy of the Rukwa rift. *Tectonophysics*, *209*, 143–158.

Kinabo, B. D., Hogan, J. P., Atekwana, E. A., Abdelsalam, M. G., & Modisi, M. P. (2008). Fault growth and propagation during incipient continental rifting: Insights from a combined aeromagnetic and Shuttle Radar Topography Mission digital elevation model investigation of the Okavango Rift Zone, northwest Botswana. *Tectonics*, *27*, TC3013. https://doi.org/10.1029/2007TC002154

Kirkpatrick, J. D., Bezerra, F. H. R., Shipton, Z. K., Do Nascimento, A. F., Pytharouli, S. I., Lunn, R. J., & Soden, A. M. (2013). Scale-dependent influence of pre-existing basement shear zones on rift faulting: a case study from NE Brazil. *Journal of the Geological Society*, *170*(2), 237–247. https://doi.org/10.1144/jgs2012-043

Korenaga, J., Holbrook, W. S., Kent, G. M., Kelemen, P. B., Detrick, R. S., Larsen, H. C., et al. (2000). Crustal structure of the southeast Greenland margin from joint refraction and reflection seismic tomography. *Journal of Geophysical Research*, *105*(B9), 21,591–21,614. https://doi.org/10.1029/2000JB900188

Kreuser, T., Wopfner, H., Kaaya, C. Z., Markwort, S., Semkiwa, P. M., & Aslandis, P. (1990). Depositional evolution of Permo-Triassic Karoo basins in Tanzania with reference to their economic potential. *Journal of African Earth Sciences*, *10*, 151–167.

Laó-Dávila, D. A., Al-Salmi, H. S., Abdelsalam, M. G., & Atekwana, E. A. (2015). Hierarchical segmentation of the Malawi Rift: The influence of inherited lithospheric heterogeneity and kinematics in the evolution of continental rifts. *Tectonics*, *34*, 2399–2417. https://doi.org/10.1002/2015TC003953

Lyons, R. P., Scholz, C. A., Buoniconti, M. R., & Martin, M. R. (2011). Late Quaternary stratigraphic analysis of the Lake Malawi Rift, East Africa: An integration of drill-core and seismic-reflection data. *Paleogeography, Palaeoclimatology, Palaeoecology*, *303*(1-4), 20–37. https://doi.org/10.1016/j.palaeo.2009.04.014

Manighetti, I., King, G. C. P., Gaudemer, Y., Scholz, C. H., & Doubre, C. (2001). Slip accumulation and lateral propagation of active normal faults in Afar. *Journal of Geophysical Research*, *106*, 13,667–16,396. https://doi.org/10.1029/2000JB900471

McCartney, T., & Scholz, C. A. (2016). A 1.3 million year record of synchronous faulting in the hangingwall and border fault of a half-graben in the Malawi (Nyasa) Rift. *Journal of Structural Geology*, *91*(C), 114–129. https://doi.org/10.1016/j.jsg.2016.08.012

McCartney, T., Scholz, C. A., Shillington, D. J., Ebinger, C. J., Accardo, N. J., Chindandali, P. R. N., et al. (2016, December). Implications of longlived intrabasin faulting in the hangingwall of the 120 km long border fault of the deeply subsided central basin of the Malawi (Nyasa) Rift. Presented at the American Geophysical Union Fall Meeting.

McConnell, B. B. (1972). Geological development of the rift system of Eastern Africa. *Geological Society of America Bulletin*, *83*, 2549–2572.

Mesko, G. T., Class, C., Maqway, M. D., Boniface, N., Manya, S., & Hemming, S. R. (2014. December). The timing of early magmatism and extension in the Southern East African Rift: Tracking geochemical source variability with 40Ar/39Ar Geochronology at the Rungwe Volcanic Province, SW Tanzania. Presented at the American Geophysical Union Fall Meeting.

Moeller, S., Grevemeyer, I., Ranero, C. R., Berndt, C., Klaeschen, D., Sallares, V., et al. (2013). Early-stage rifting of the northern Tyrrhenian Sea Basin: Results from a combined wide-angle and multichannel seismic study. *Geochemistry, Geophysics, Geosystems*, *14*, 3032–3052. https://doi.org/10.1002/ggge.20180

Morley, C. K. (1988). Variable extension in Lake Tanganyika. *Tectonics*, *7*(4), 785–801. https://doi.org/10.1029/TC007i004p00785

Morley, C. K. (1999). Patterns of displacement along large normal faults: Implications for basin evolution and fault propagation, based on examples from East Africa. *American Association of Petroleum Geologists*, *83*, 613–634.

Morley, C. K. (2002). Evolution of large normal faults: Evidence from seismic reflection data. *American Association of Petroleum Geologists*, *86*(6), 961–978.

Morley, C. K. (2010). Stress re-orientation along zones of weak fabrics in rifts: An explanation for pure extension in "oblique" rift segments? *Earth and Planetary Science Letters*, *297*(3-4), 667–673. https://doi.org/10.1016/j.epsl.2010.07.022

Morley, C. K., Cunningham, S. M., Harper, R. M., & Wescott, W. A. (1992). Geology and geophysics of the Rukwa Rift, East Africa. *Tectonics*, *11*, 69–81. https://doi.org/10.1029/91TC02102

Morley, C. K., Nelson, R. A., Patton, T. L., & Munn, S. G. (1990). Transfer zones in the East African Rift system and their relevance to hydrocarbon exploration in rifts. *American Association of Petroleum Geologists*, *74*(8), 1234–1253.

Mortimer, E., Kirstein, L. A., Stuart, F. M., & Strecker, M. R. (2016). Spatio-temporal trends in normal-fault segmentation recorded by low-temperature thermochronology: Livingstone fault scarp, Malawi Rift, East African Rift system. *Earth and Planetary Science Letters*, *455*(C), 62–72. https://doi.org/10.1016/j.epsl.2016.08.040

Mortimer, E., Paton, D. A., Scholz, C. A., Strecker, M. R., & Blisniuk, P. (2007). Orthogonal to oblique rifting: Effect of rift basin orientation in the evolution of the North basin, Malawi Rift, East Africa. *Basin Research*, *19*(3), 393–407. https://doi.org/10.1111/j.1365-2117.2007.00332.x

Mortimer, E. J., Paton, D. A., Scholz, C. A., & Strecker, M. R. (2016). Implications of structural inheritance in oblique rift zones for basin compartmentalization: Nkhata Basin, Malawi Rift (EARS). *Marine and Petroleum Geology*, *72*(C), 110–121. https://doi.org/10.1016/j.marpetgeo.2015.12.018

Nicholson, S. E., Klotter, D., & Chavula, G. (2013). A detailed rainfall climatology for Malawi, Southern Africa. *International Journal of Climatology*, *34*(2), 315–325. https://doi.org/10.1002/joc.3687

Nicol, A., Walsh, J., Berryman, K., & Nodder, S. (2005). Growth of a normal fault by the accumulation of slip over millions of years. *Journal of Structural Geology*, *27*(2), 327–342. https://doi.org/10.1016/j.jsg.2004.09.002

Nixon, C. W., McNeill, L. C., Bull, J. M., Bell, R. E., Gawthorpe, R. L., Henstock, T. J., et al. (2016). Rapid spatiotemporal variations in rift structure during development of the Corinth Rift, central Greece. *Tectonics*, *35*, 1225–1248. https://doi.org/10.1002/2015TC004026

Nyblade, A. A., & Brazier, R. A. (2002). Precambrian lithospheric controls on the development of the East African rift system. *Geology*, *30*(8), 755–758.

Olive, J.-A., Behn, M. D., & Malatesta, L. C. (2014). Modes of extensional faulting controlled by surface processes. *Geophysical Research Letters*, *41*, 6725–6733. https://doi.org/10.1002/2014GL061507

Paul, D., & Mitra, S. (2013). Experimental models of transfer zones in rift systems. *AAPG Bulletin*, *97*(5), 759–780. https://doi.org/10.1306/10161212105

Peirce, J. W., & Lipkov, L. (1988). Structural interpretation of the Rukwa RIFT, Tanzania. *Geophysics*, *53*, 824–836.

Pérez-Gussinyé, M., Metois, M., Fernández, M., Vergés, J., Fullea, J., & Lowry, A. R. (2009). Effective elastic thickness of Africa and its relationship to other proxies for lithospheric structure and surface tectonics. *Earth and Planetary Science Letters*, *287*(1-2), 152–167. https://doi.org/10.1016/j.epsl.2009.08.004

Pinna, P., Muhongo, S. M., Mcharo, B. A., Le Goff, E., Deschamps, Y., Ralay, F., & Milesi, J. P. (2004). Geology and mineral map of Tanzania. BRGM.

Rasskazov, S. V., Logachev, N. A., Ivanov, A. V., Boven, A. A., Maslovskaya, M. N., Saranina, E. V., et al. (2003). A magmatic episode in the western rift of East Africa (19-17 Ma). *Geologiya i Geofizika*, *44*(4), 317–324.

Reeve, M. T., Bell, R. E., Duffy, O. B., Jackson, C. A. L., & Sansom, E. (2015). The growth of non-colinear normal fault systems; What can we learn from 3D seismic reflection data? *Journal of Structural Geology*, *70*(C), 141–155. https://doi.org/10.1016/j.jsg.2014.11.007

Ring, U. (1994). The influence of preexisting structure on the evolution of the Cenozoic Malawi rift (East African rift system). *Tectonics*, *13*, 313–326. https://doi.org/10.1029/93TC03188

Roberts, E. M., O'Connor, P. M., Gottfried, M. D., Stevens, N., Kapalima, S., & Ngasala, S. (2004). Revised stratigraphy and age of the Red Sandstone Group in the Rukwa Rift Basin, Tanzania. *Cretaceous Research*, *25*(5), 749–759. https://doi.org/10.1016/j.cretres.2004.06.007

Roberts, E. M., O'Connor, P. M., Stevens, N. J., Gottfried, M. D., Jinnah, Z. A., Ngasala, S., et al. (2010). Sedimentology and depositional environments of the Red Sandstone Group, Rukwa Rift Basin, southwestern Tanzania: New insight into Cretaceous and Paleogene terrestrial ecosystems and tectonics in sub-equatorial Africa. *Journal of African Earth Sciences*, 179–212. https://doi.org/10.1016/j.jafrearsci.2009.09.002

Roberts, E. M., Stevens, N. J., & O'Connor, P. M. (2012). Initiation of the western branch of the East African Rift coeval with the eastern branch. *Nature Geoscience*, *5*(4), 289–294. https://doi.org/10.1038/ngeo1432

Rosendahl, B. R. (1987). Architecture of continental rifts with special reference to East Africa. *Annual Reviews in Earth and Planetary Science*, *15*, 445–503.

Rosendahl, B. R., Kilembe, E., & Kaczmarick, K. (1992). Comparison of the Tanganyika, Malawi, Rukwa and Turkana Rift zones from analyses of seismic-reflection data. *Tectonophysics*, *213*(1-2), 235–256. https://doi.org/10.1016/0040-1951(92)90261-4

Saria, E., Calais, E., Stamps, D. S., Delvaux, D., & Hartnady, C. J. H. (2014). Present-day kinematics of the East African Rift. *Journal of Geophysical Research: Solid Earth*, *119*, 3584–3600. https://doi.org/10.1002/(ISSN)2169-9356

Schlische, R. W., Young, S. S., Ackermann, R. V., & Gupta, A. (1996). Geometry and scaling relations of a population of very small rift-related normal faults. *Geology*, *24*, 683–686.

Scholz, C. A. (1989). *Seismic atlas of Lake Malawi (Nyasa)*. East Africa: Project PROBE.

Scholz, C. A. (1995a). Seismic stratigraphy of an accommodation-zone margin rift-lake delta, Lake Malawi, Africa. In J. J. Lambiase (Ed.), *Hydrocarbon habitat in rift basins* (pp. 183–195). London: Geological Society.

Scholz, C. A. (1995b). Deltas of the Lake Malawi Rift, East Africa: Seismic expression and exploration implications. *AAPG Bulletin*, *79*(11), 1679–1697.

Scholz, C. A., Cohen, A. S., Johnson, T. C., King, J., Talbot, M. R., & Brown, E. T. (2011). Scientific drilling in the Great Rift Valley: The 2005 Lake Malawi Scientific Drilling Project—An overview of the past 145,000 years of climate variability in Southern Hemisphere East Africa. *Paleogeography, Palaeoclimatology, Palaeoecology*, *303*(1-4), 3–19. https://doi.org/10.1016/j.palaeo.2010.10.030

Scholz, C. H., & Contreras, J. C. (1998). Mechanics of continental rift architecture. *Geology*, *26*(11), 967–970.

Shillington, D. J., Chindandali, P. R. N., Scholz, C., Ebinger, C., Onyango, E., Peterson, K., et al. (2016, December). Active intra-basin faulting in the Northern Basin of Lake Malawi from seismic reflection data. Presented at the American Geophysical Union Fall Meeting.

Shillington, D. J., Gaherty, J. B., Ebinger, C. J., Scholz, C. A., Selway, K., Nyblade, A. A., et al. (2016). Acquisition of a unique onshore/offshore geophysical and geochemical dataset in the Northern Malawi (Nyasa) Rift. *Seismological Research Letters*, *87*(6), 1–11. https://doi.org/10.1785/0220160112

Smith, M., & Mosley, P. (1993). Crustal heterogeneity and basement influence on the development of the Kenya Rift, East Africa. *Tectonics*, *12*, 591–606. https://doi.org/10.1029/92TC01710

Soreghan, M. J., Scholz, C. A., & Wells, J. T. (1999). Coarse-grained, deep-water sedimentation along a border fault margin of Lake Malawi, Africa: Seismic stratigraphic analysis. *Journal of Sedimentary Research*, *69*(4), 832–846.

Specht, T. D., & Rosendahl, B. R. (1989). Architecture of the Lake Malawi Rift, East Africa. *Journal of African Earth Sciences*, *8*, 355–382.

Stamps, D. S., Flesch, L. M., Calais, E., & Ghosh, A. (2014). Current kinematics and dynamics of Africa and the East African Rift system. *Journal of Geophysical Research: Solid Earth*, *119*, 5161–5186. https://doi.org/10.1002/(ISSN)2169-9356

Theunissen, K., Klerkx, J., Melnikov, A., & Mruma, A. (1996). Mechanisms of inheritance of rift faulting in the western branch of the East African Rift, Tanzania. *Tectonics*, *15*(4), 776–790. https://doi.org/10.1029/95TC03685

Tommasi, A., & Vauchez, A. (2001). Continental rifting parallel to ancient collisional belts: An eject of the mechanical anisotropy of the lithospheric mantle. *Earth and Planetary Science Letters*, *185*, 199–201.

Upcott, N. M., Mukasa, R. K., Ebinger, C. J., & Karner, G. D. (1996). Along-axis segmentation and isostasy in the Western rift, East Africa. *Journal of Geophysical Research*, *101*(B2), 3247–3268. https://doi.org/10.1029/95JB01480

Verschuur, D. J., Berkhout, A. J., & Wapenaar, C. P. A. (1992). Adaptive surface-related multiple elimination. *Geophysics*, *57*(9), 1166–1177.

Versfelt, J., & Rosendahl, B. R. (1989). Relationships between pre-rift structure and rift architecture in Lakes Tanganyika and Malawi, East Africa. *Nature*, *337*(6205), 354–357. https://doi.org/10.1038/337354a0

Vidale, J. E. (1990). Finite-difference calculation of traveltimes in three dimensions. *Geophysics*, *55*(5), 521–526.

Walsh, J. J., Nicol, A., & Childs, C. (2002). An alternative model for the growth of faults. *Journal of Structural Geology*, *24*, 1669–1675.

Watremez, L., Helen Lau, K. W., Nedimović, M. R., & Louden, K. E. (2015). Traveltime tomography of a dense wide-angle profile across Orphan Basin *Geophysics*, *80*(3), B69–B82. https://doi.org/10.1190/geo2014-0377.1

Wescott, W. A., Krebs, W. N., Engelhardt, D. W., & Cunningham, S. M. (1991). New biostratigraphic age dates from the Lake Rukwa Rift Basin in Western Tanzania. *American Association of Petroleum Geologists*, *75*, 1255–1263.

Wheeler, W. H., & Karson, J. A. (1989). Structure and kinematics of the Livingstone Mountains border fault zone, Nyasa (Malawi) Rift, southwestern Tanzania. *Journal of African Earth Sciences*, *8*, 393–413.

Wheeler, W. H., & Rosendahl, B. R. (1994). Geometry of the Livingstone Mountains Border Fault, Nyasa (Malawi) Rift, East Africa. *Tectonics*, *13*, 303–312. https://doi.org/10.1029/93TC02314

Wölbern, I., Rümpker, G., Schumann, A., & Muwanga, A. (2010). Crustal thinning beneath the Rwenzori region, Albertine rift, Uganda, from receiver-function analysis. *International Journal of Earth Sciences*, *99*(7), 1545–1557. https://doi.org/10.1007/s00531-009-0509-2

Wopfner, H. (2002). Tectonic and climatic events controlling deposition in Tanzanian Karoo basins. *Journal of African Earth Sciences*, *34*, 167–177.

Zelt, C. A. (1999). Modelling strategies and model assessment for wide-angle seismic traveltime data. *Geophysical Journal International*, *139*, 183–204.

Zelt, C. A., & Barton, P. J. (1998). Three-dimensional seismic refraction tomography: A comparison of two methods applied to data from the Faeroe Basin. *Journal of Geophysical Research*, *103*(4), 7187–7210. https://doi.org/10.1029/97JB03536

Zhang, J., & Toksoz, M. N. (1998). Nonlinear refraction traveltime tomography. *Geophysics*, *63*(5), 1726–1737.